CrossMark

A Particle Module for the PLUTO Code. II. Hybrid Framework for Modeling Nonthermal Emission from Relativistic Magnetized Flows

Bhargav Vaidya[1,2] , Andrea Mignone[2], Gianluigi Bodo[3] , Paola Rossi[3] , and Silvano Massaglia[2]
[1] Centre of Astronomy, Indian Institute of Technology Indore, Khandwa Road, Simrol, Indore 453552, India; bvaidya@iiti.ac.in
[2] Dipartimento di Fisica, University of Torino, via Pietro Giuria 1, I-10125 Torino, Italy
[3] INAF, Osservatorio Astrofisico di Torino, Strada Osservatorio 20, I-10025 Pino Torinese, Italy

Abstract

We describe a new hybrid framework to model non-thermal spectral signatures from highly energetic particles embedded in a large-scale classical or relativistic magnetohydrodynamic (MHD) flow. Our method makes use of *Lagrangian* particles moving through an Eulerian grid where the (relativistic) MHD equations are solved concurrently. Lagrangian particles follow fluid streamlines and represent ensembles of (real) relativistic particles with a finite energy distribution. The spectral distribution of each particle is updated in time by solving the relativistic cosmic ray transport equation based on local fluid conditions. This enables us to account for a number of physical processes, such as adiabatic expansion, synchrotron and inverse Compton emission. An accurate semi-analytically numerical scheme that combines the method of characteristics with a Lagrangian discretization in the energy coordinate is described. In the presence of (relativistic) magnetized shocks, a novel approach to consistently model particle energization due to diffusive shock acceleration is presented. Our approach relies on a refined shock-detection algorithm and updates the particle energy distribution based on the shock compression ratio, magnetic field orientation, and amount of (parameterized) turbulence. The evolved distribution from each Lagrangian particle is further used to produce observational signatures like emission maps and polarization signals, accounting for proper relativistic corrections. We further demonstrate the validity of this hybrid framework using standard numerical benchmarks and evaluate the applicability of such a tool to study high-energy emission from extragalactic jets.

Key words: acceleration of particles – methods: numerical – polarization – radiation mechanisms: non-thermal – relativistic processes – shock waves

1. Introduction

Magnetized and relativistic large-scale flows in the form of jets are a common observational feature seen for example in active galactic nuclei (AGNs), gamma-ray bursts, and micro-quasars. The dominant emission is originated by non-thermal processes from high-energy particles. Multi-wavelength observations covering a wide spectrum from radio wavelengths to TeV gamma-ray emission provide valuable insights into the micro-physical processes that occur in jets and lead to the observed radiation. The length scales associated with these micro-physical processes are many orders of magnitude smaller than the physical jet scales, which can range up to few tens of kiloparsecs. Connecting a bridge between these scales poses a serious challenge to theoretical modeling of the emission from AGN jets. In the present work, we aim to build a quantitative connection between such disjoint scales by developing a numerical tool that can simulate multi-dimensional flow patterns, treating small-scale processes in a sub-grid manner. We describe such a tool which consistently accounts for most of the micro-physical processes.

The general analytical picture of multi-wavelength radiation from beamed relativistic magnetized jets was proposed by, e.g., Blandford & Königl (1979), Marscher (1980) and Konigl (1981). Since then, synchrotron emission signatures from large-scale jets have been obtained from time-dependent simulations through post-processing. In the relativistic hydrodynamic context, transfer functions between thermal and non-thermal electrons in the jet are used (Gómez et al. 1995, 1997; Aloy et al. 2000) whereas in the case of relativistic magnetohydrodynamic (MHD) calculations,

the magnetic structure inside the jet is used to compute synchrotron emission maps (e.g., Porth et al. 2011; Hardcastle & Krause 2014; English et al. 2016).

Formalisms for studying the micro-physics of particle acceleration at shocks using hybrid implementations combining both particles and grid-based fluid descriptions have also been developed targeting different scales of interest. At the scale of the electron's gyro-radius, the most consistent approach is that of particle in cell (PIC). Several groups have applied this kinetic approach to understand shock acceleration at relativistic shocks (e.g., Sironi et al. 2015 and references therein). A hybrid MHD–PIC approach can be used to study the shock acceleration phenomenon on slightly large length scales, typically of the order of a few thousand proton gyro-scales. Such an approach, developed by, e.g., Bai et al. (2015), Mignone et al. (2018) and van Marle et al. (2018) describes the interaction between collisionless cosmic ray particles and a thermal plasma. Similarly, Daldorff et al. (2014) proposed a hybrid approach for the BATS-R-US code that combines Hall–MHD and PIC methods to capture small-scale kinetic effects in magnetosphere simulations.

An alternative approach in the numerical modeling of non-thermal emission from astrophysical jets treats the population of non-thermal electrons as separate particle entities suspended in fluid. Effects due to synchrotron aging in the presence of shock acceleration under the test particle limit were studied for radio galaxies using multi-dimensional classical MHD simulations by Jones et al. (1999) and Tregillis et al. (2001). Acceleration of test particles and subsequent radiative losses in the presence of shocks formed via hydrodynamic Kelvin–Helmholtz vortices

were studied by Micono et al. (1999). Such a hybrid framework of combining test particles with classical fluid has also been used effectively to study cosmic-ray transport in a cosmological context (Miniati 2001). For relativistic hydrodynamic flows, populations of non-thermal particles (NTPs) were included to study non-thermal emission from internal shocks in blazars (Mimica et al. 2009; Mimica & Aloy 2012; Fromm et al. 2016). Recent relativistic hydrodynamical simulations using NTPs have also been applied for a study of star–jet interactions in AGNs (de la Cita et al. 2016). There are two critical limitations with models using NTPs. First, as the fluid simulations are done with relativistic hydrodynamics, magnetic field strengths are assumed to be in equipartition with the internal energy density. This ad hoc parameterized assumption of magnetic field strengths can affect the estimation of the spectral break in the particle distribution due to synchrotron processes. The second simplifying assumption in these models is the choice of a constant value for the power-law index $\mathcal{N}(E) \propto E^{-m}$, ($m = 2.0$; de la Cita et al. 2016, and $m = 2.23$; Fromm et al. 2016) in the recipe of particle injection at shocks.

In the present work, we describe methods used to overcome the above limitations with the aim of building a state-of-the-art hybrid framework of particle transport to model high-energy, non-thermal emission from large-scale 3D relativistic MHD (RMHD) simulations. Our sub-grid model for shock acceleration incorporates the dependence of the spectral index on the shock strength and magnetic field orientation. The magnetic fields obtained from our RMHD simulations are used to compute radiation losses due to synchrotron and inverse Compton (IC) emission in a more accurate manner without any assumption on equipartition. Further, we also incorporate the effects of relativistic aberration in estimating the polarized emission due to synchrotron processes.

Unlike the MHD-PIC approach (Bai et al. 2015; Mignone et al. 2018; van Marle et al. 2018), we do not consider the feedback of motion of particles on the fluid. This prevents us from studying the associated nonlinear coupling effects. However, we can certainly extend the applicability of the presented hybrid framework to observable scales, whereby micro-physical aspects of spectral evolution are treated using sub-grid physics based on local fluid conditions. Further, we have only considered the spectral evolution for electrons in the presence of magnetic fields and shocks. Modifications in the mass and timescales would be required if the physics of acceleration of protons were to be incorporated. Also, protons are expected to undergo from a negligible amount of synchrotron loss in comparison with electrons, which would significantly affect their spectral behavior. Additionally, the post-shock spectral evolution is different for protons as demonstrated by PIC simulations for all kinds of shocks (e.g., Sironi et al. 2013; Park et al. 2015; Marcowith et al. 2016). This sub-grid physics associated with acceleration and radiative loss of protons is not included in the present work.

The paper is organized as follows: a detailed theoretical description of our hybrid particle and fluid framework is presented in Section 2. In particular, the transport equation for particle spectral evolution is given in Section 2.1, details of numerical implementation are outlined in Section 2.3, and the different micro-physical processes considered are elaborated in detail in Sections 2.2 and 2.4. The post-processing methods used to obtain emissivity and polarization signatures from

particles are described in Section 3. In Section 4, we demonstrate the accuracy of the developed hybrid framework using standard tests and go on to describe the astrophysical applications in Section 5.

2. Numerical Framework

2.1. The Cosmic Ray Transport Equation

The transport equation for cosmic rays in a scattering medium has been derived, in the classical case, by several authors (see e.g., Parker 1965; Jokipii & Parker 1970; Skilling 1975; Webb & Gleeson 1979) and, in the relativistic case, by Webb (1989). Let $f_0(x^\mu, p)$ be the isotropic distribution function of the NTP in phase space, where x^μ and p denote the position four-vector and the momentum magnitude, respectively; the transport equation then reads (Webb 1989)

$$\nabla_\mu(u^\mu f_0 + q^\mu) + \frac{1}{p^2}\frac{\partial}{\partial p}\left[-\frac{p^3}{3}f_0\nabla_\mu u^\mu + \langle\dot{p}\rangle_l f_0 \right.$$
$$\left. - \Gamma_{\text{visc}}p^4\tau\frac{\partial f_0}{\partial p} - p^2 D_{pp}\frac{\partial f_0}{\partial p} - p(p^0)^2\dot{u}_\mu q^\mu\right] = 0 \qquad (1)$$

where the terms in round brackets describe particle transport by convection, and particle transport by diffusion. Here u^μ is the bulk four-velocity of the surrounding fluid while q^μ is the spatial diffusion flux. The terms in square brackets are responsible for evolution in momentum space and describe

1. the energy changes due to adiabatic expansion;
2. the losses associated with synchrotron and IC emission (here $\langle\dot{p}\rangle_l$ is the average momentum change due to non-thermal radiation), see Section 2.2;
3. the acceleration term due to fluid shear, where Γ_{visc} is the shear viscosity coefficient;
4. the Fermi second-order process, where D_{pp} is the diffusion coefficient in momentum space;
5. the non-inertial energy changes associated with the fact that particle momentum p is measured relative to a local Lorentz frame moving with the fluid (here p^0 is the temporal component of the momentum four-vector while $\dot{u}_\mu$ is the four-acceleration).

For the present purpose, we shall neglect particle transport due to spatial diffusion, (i.e., $q^\mu = 0$) and, for simplicity, ignore particle energization due to shear ($\Gamma_{\text{visc}} = 0$), Fermi second-order processes ($D_{pp} = 0$), and the last term involving non-inertial energy changes (as $q^\mu = 0$). Equation (1) then reduces to

$$\nabla_\mu(u^\mu f_0) + \frac{1}{p^2}\frac{\partial}{\partial p}\left[-\frac{p^3}{3}f_0\nabla_\mu u^\mu + \langle\dot{p}\rangle_l f_0\right] = 0. \qquad (2)$$

On expanding the derivative in the first term and using the fact that

$$u^\mu\nabla_\mu = \gamma\left(\frac{\partial}{\partial t} + v^i\frac{\partial}{\partial x_i}\right) \equiv \frac{d}{d\tau} \qquad (3)$$

is the Lagrangian derivative with respect to proper time, related to the laboratory time by $d\tau = dt/\gamma$, where γ is the bulk

Lorentz factor, we obtain

$$p^2 \frac{df_0}{d\tau} + \frac{\partial}{\partial p}\left[-\frac{p^3}{3}f_0 \nabla_\mu u^\mu + \langle \dot{p} \rangle_l f_0 \right] = -p^2 f_0 \nabla_\mu u^\mu. \quad (4)$$

We now define $\mathcal{N}(p, \tau) = \int d\Omega p^2 f_0 \approx 4\pi p^2 f_0$, taking into account the assumption of isotropy for distribution of particles in momentum space. Physically, $\mathcal{N}(p, t)dp$ represents the number of particles per unit volume lying in the range from p to $p+dp$ at a given time t. Since the particles are highly relativistic, we can express the energy of the particle as $E \approx pc$ (c being the speed of light) and therefore, $\mathcal{N}(E, \tau)dE = \mathcal{N}(p, \tau)dp$. Integrating Equation (4) over the solid angle yields

$$\frac{d\mathcal{N}}{d\tau} + \frac{\partial}{\partial E}\left[\left(-\frac{E}{3}\nabla_\mu u^\mu + \dot{E}_l\right)\mathcal{N}\right] = -\mathcal{N}\nabla_\mu u^\mu \quad (5)$$

where the first term in square brackets accounts for energy losses from adiabatic expansion while the second term $\dot{E}_l = \langle \dot{p} \rangle_l/p^2$ is the radiative loss term due to synchrotron and IC processes.

2.2. Radiative Losses

Energetic electrons lose energy by *synchrotron* emission in the presence of magnetic fields and by the IC process up-scattering the surrounding radiation field. For the latter process we assume that the scattering in the relativistic particle rest frame is Thompson, so that the cross section σ_T is independent of the incident photon energy E_{ph}. The energy loss terms for electrons with isotropically distributed velocity vectors is therefore given by

$$\dot{E}_l = -c_r E^2 \quad (6)$$

where

$$c_r = \frac{4}{3}\frac{\sigma_T c \beta^2}{m_e^2 c^4}[U_B(t) + U_{rad}(E_{ph}, t)], \quad (7)$$

where β is the velocity of the electrons (we assume $\beta = 1$ for highly relativistic electrons) and m_e is their mass. The quantities $U_B = \frac{B^2}{8\pi}$ and U_{rad} are the magnetic and the radiation field energy densities, respectively. For the present work, we use the isotropic cosmic microwave background (CMB) as the radiation source. Therefore, applying the blackbody approximation, we have $U_{rad} = a_{rad}T_{CMB}^4 = a_{rad}T_0^4(1 + z)^4$ where a_{rad} is the radiation constant, z is the redshift and $T_0 = 2.728$ K is the temperature of CMB at the present epoch.

2.3. Numerical Implementation

Equation (5) is solved using a particle approach where a large number of Lagrangian (or macro-) particles sample the distribution function in physical space. A macro-particle represents an ensemble of actual particles (leptons or hadrons) that are very close in physical space but with a finite distribution in energy (or momentum) space. To each macro-particle we associate a time-dependent energy distribution function $\mathcal{N}_p(E, \tau)$ quantized in discrete energy bins.

For numerical purposes, however, it is more convenient to rewrite Equation (5) by introducing the number density ratio $\chi_p = \mathcal{N}_p/n$, which represents the number density of electrons normalized to the fluid number density. Using the continuity equation, $\nabla_\mu(nu^\mu) = 0$, it is straightforward to show that χ_p obeys the following equation:

$$\frac{d\chi_p}{d\tau} + \frac{\partial}{\partial E}\left[\left(-\frac{E}{3}\nabla_\mu u^\mu + \dot{E}_l\right)\chi_p\right] = 0. \quad (8)$$

The solution of Equation (8) is carried out separately into a transport step (during which we update the spatial coordinates of the particles) followed by a spectral evolution step (corresponding to the evolution of the particle energy distribution). These two steps are now described.

2.3.1. Transport Step

Since the distribution function is carried along with the fluid, the spatial part of Equation (8) is solved by advancing the macro-particle coordinates x_p through the ordinary differential equations

$$\frac{dx_p}{dt} = v(x_p), \quad (9)$$

where v represents the fluid velocity interpolated at the macro-particle position and the subscript p labels the particle. Equation (9) is solved concurrently with the fluid equations given by

$$\frac{\partial U}{\partial t} + \nabla \cdot F = S \quad (10)$$

which are solved as usual by means of the standard Godunov methods already present in the PLUTO code (Mignone et al. 2007, 2012). In the equation above, U is an array of conservative variables, F is the flux tensor while S denotes the source terms.

The same time-marching scheme used for the fluid is also employed to update the particle position. For example, in a second-order Runge–Kutta scheme, a single time update consists of a predictor step followed by a corrector step.

1. *Predictor step*: particles and conservative fluid quantities are first evolved for a *full* step according to

$$\begin{cases} x_p^* = x_p^n + \Delta t^n v^n(x_p^n) \\ U^* = U^n - \Delta t^n(\nabla \cdot F)^n \end{cases} \quad (11)$$

where Δt^n is the current level time step, x_p^n denotes the particle's position at time step n and $v^n(x_p^n)$ is the fluid velocity interpolated at the particle position (at the current time level).

2. *Corrector step*: using the fluid velocity field obtained at the end of the predictor step, particles and fluid are advanced to the next time level using a trapezoidal rule:

$$\begin{cases} x_p^{n+1} = x_p^n + \frac{\Delta t}{2}[v^n(x_p^n) + v^*(x_p^*)] \\ U^{n+1} = U^n - \frac{\Delta t}{2}[(\nabla \cdot F)^n + (\nabla \cdot F)^*] \end{cases} \quad (12)$$

where $v^*(x_p^*)$ denotes the (predicted) fluid velocity interpolated at the (predicted) particle position.

Interpolation of fluid quantities at the particle position is carried out by means of standard techniques used in PIC codes

(see, e.g., Birdsall & Langdon 2004):

$$v(x_\mathrm{p}) = \sum_{ijk} W(x_{ijk} - x_\mathrm{p})v_{ijk} \qquad (13)$$

where $W(x_{ijk} - x_\mathrm{p}) = W(x_i - x_\mathrm{p})W(y_j - y_\mathrm{p})W(z_k - z_\mathrm{p})$ is the product of three one-dimensional weighting functions, while the indices i, j, and k span the computational (fluid) grid. For the present implementation we employ the standard second-order accurate triangular shaped cloud method.

Particles are stored in memory as a doubly linked list in which each node is a C data-structure containing all of the particle attributes. Parallel implementation is based on the Message Passing Interface and employs standard domain decomposition based on the fluid grid. Particles are therefore distributed according to their physical location and are thus owned by the processor hosting them. Parallel scaling up to 10^4 processors has been demonstrated in a previous work; see Vaidya et al. (2016).

2.3.2. Spectral Evolution Step

As macro-particles are transported in space by the fluid, their spectral distribution evolves according to the energy part of Equation (8) which can be regarded as a homogeneous scalar conservation law with variable coefficients in (E, τ) space. Here we show that a semi-analytical solution can be obtained using the method of characteristics. The resulting expressions can then be used to advance the spectral energy distribution of the particles using a Lagrangian scheme in which the discrete energy grid points change in time.

To this purpose, we first observe that the characteristic curves of Equation (8) are given by

$$\frac{dE}{d\tau} = -c_a(\tau)E - c_r(\tau)E^2 \equiv \dot{E}, \qquad (14)$$

where $c_a(\tau) = \nabla_\mu u^\mu / 3$, while $c_r(\tau)$ is given in Equation (7). Integrating Equation (14) for $\tau \geqslant \tau_0$, one finds

$$E(\tau) = \frac{E_0 e^{-a(\tau)}}{1 + b(\tau)E_0}, \qquad (15)$$

where E_0 is the initial energy coordinate while

$$a(\tau) = \int_{\tau_0}^{\tau} c_a(\tau)d\tau, \quad b(\tau) = \int_{\tau_0}^{\tau} c_r(\tau)e^{-a(\tau)}d\tau. \qquad (16)$$

Along the characteristic curve, Equation (8) becomes an ordinary differential equation so that, for each macro-particle, we solve

$$\left.\frac{d\chi_\mathrm{p}}{d\tau}\right|_{\mathcal{C}} = -\left(\frac{\partial \dot{E}}{\partial E}\right)\chi_\mathrm{p}, \qquad (17)$$

where $\dot{E}$ is given by Equation (14) while the subscript $\mathcal{C}$ on the left-hand side denotes differentiation along the characteristic curve. Integrating Equation (17) and considering the fact that $\dot{E}$ is a function of E alone, one finds

$$\chi_\mathrm{p}(E, \tau)dE = \chi_{\mathrm{p}0}dE_0, \qquad (18)$$

where $\chi_{\mathrm{p}0} = \chi_\mathrm{p}(E_0, \tau_0)$. The previous expression shows that the number of particles (normalized to the fluid density) per energy interval remains constant as the interval changes in time. The term dE_0/dE describes the spreading or shrinking of

the energy interval and it is readily computed from Equation (15). Integrating Equation (18) one has

$$\chi_\mathrm{p}(E(\tau), \tau) = \chi_{\mathrm{p}0}[1 + b(\tau)E_0]^2\left(\frac{n(\tau)}{n_0}\right)^{-1/3}, \qquad (19)$$

where $n_0 = n(\tau_0)$ and where we have used

$$e^{a(\tau)} = \exp\left(-\int_{\tau_0}^{\tau}\frac{d\log n}{3}\right) = \left(\frac{n(\tau)}{n_0}\right)^{-1/3}. \qquad (20)$$

The previous analytical expressions can be used to construct a numerical scheme based on a Lagrangian solution update. To this purpose, we discretize (for each macro-particle) the energy space into N_E energy bins of width $\Delta E_i^n = E_{i+\frac{1}{2}}^n - E_{i-\frac{1}{2}}^n$ (where $i = 1, \ldots, N_E$ while the superscript n denotes the temporal index) spanning from E_min^n to E_max^n. In our Lagrangian scheme, mesh interface coordinates are evolved in time according to Equation (15) which we conveniently rewrite (using Equation (20)) as

$$E_{i+\frac{1}{2}}^{n+1} = \frac{E_{i+\frac{1}{2}}^n}{1 + b^{n+1}E_{i+\frac{1}{2}}^n}\left(\frac{\rho^{n+1}}{\rho^n}\right)^{1/3}. \qquad (21)$$

The particle distribution χ_p does not need to be updated explicitly (at least away from shocks, see Section 2.4), since Equation (18) automatically ensures that the number of particles per energy interval is conserved in time:

$$\langle\chi\rangle_{\mathrm{p},i}^{n+1} = \frac{1}{\Delta E_i^{n+1}}\int_{E_{i-\frac{1}{2}}^{n+1}}^{E_{i+\frac{1}{2}}^{n+1}} \chi_\mathrm{p}^{n+1} dE = \langle\chi\rangle_{\mathrm{p},i}^n. \qquad (22)$$

This approach provides, at least formally, an exact solution update. A numerical approximation must, however, be introduced since the coefficient $b(\tau)$ (Equation (21)) has to be computed from fluid quantities at the particle position. Using a trapezoidal rule to evaluate the second integral in Equation (16) together with Equation (20) we obtain

$$b^{n+1} \approx \frac{\Delta t}{2}\left[\left(\frac{c_r}{\gamma}\right)^n + \left(\frac{c_r}{\gamma}\right)^{n+1}\left(\frac{\rho^{n+1}}{\rho^n}\right)^{1/3}\right], \qquad (23)$$

where the factor $1/\gamma$ comes from the definition of the proper time. Equation (21) with Equation (23) do not make the scheme implicit inasmuch as the spectral evolution step is performed after the fluid corrector and the particle transport step.

Our method extends the approaches of, e.g., Kardashev (1962) and Mimica & Aloy (2012) and it is essentially a Lagrangian discretization for updating the distribution function in the energy coordinate.

In all of the tests presented here we initialize $\langle\chi\rangle_\mathrm{p}$ at $t = t^0$ using an equally spaced logarithmic energy grid and a power-law distribution

$$\langle\chi\rangle_{\mathrm{p},i}^0 = \frac{\mathcal{N}_\mathrm{tot}}{n^0}\left(\frac{1 - m}{E_\mathrm{max}^{1-m} - E_\mathrm{min}^{1-m}}\right)E_i^{-m}, \qquad (24)$$

where $\mathcal{N}_\mathrm{tot}$ is the initial number density of physical particles (i.e., electrons) associated to the macro-particle p, n^0 is the initial fluid number density interpolated at the particle position and m is the electron power index.

We remark that our formalism holds if physical micro-particles embedded within a single macro-particle remain close in physical space (although they are allowed to have a distribution in energy space). Therefore, an additional constraint should be imposed on the maximum Larmor radius so that it does not exceed the computational cell size. This sets an upper threshold E_{max} to the maximum attainable energy of a given macro-particle, namely

$$E \leqslant E_{\mathrm{max}} = \gamma_L^{\mathrm{cf}} m_{\mathrm{e}} c^2 = \frac{eBr_L^{\mathrm{cf}}}{\beta_\perp} \qquad (25)$$

where $r_L^{\mathrm{cf}} = 0.5 \min(\Delta x, \Delta y, \Delta z)$ is computed at the particle cell position, B is the magnetic field in Gauss and e is electron charge in c.g.s. units. In the macro-particle limit, we assume that the individual leptons are highly relativistic and therefore the ratio of velocity of a single electron perpendicular to the magnetic field with the speed of light, $\beta_\perp \approx 1$.

The initial energy bounds, the number of particles $\mathcal{N}_{\mathrm{tot}}$, and the value of m are specified for each test presented in this paper. The Lagrangian scheme described above has the distinct advantage of reducing the amount of numerical diffusion typical of Eulerian discretizations and it does not require an explicit prescription of boundary conditions.

2.4. Diffusive Shock Acceleration

The mechanism of diffusive shock acceleration (DSA) plays an important role in particle acceleration in a wide variety of astrophysical environments, particularly in supernova remnants, AGN jets, gamma-ray bursts (GRBs), solar corona, etc. The steady state theory of DSA naturally results in a power-law spectral distribution (e.g., Blandford & Ostriker 1978; Drury 1983; Kirk et al. 2000; Achterberg et al. 2001) The two most important factors on which the post-shock particle distribution depends on are the strength of the magnetized shock (i.e., the compression ratio) and the orientation of magnetic field lines with respect to the shock normal. The obliquity of magnetized shocks plays a very important role in determining the post-shock particle distribution (e.g., Jokipii 1987; Ballard & Heavens 1991). A comprehensive treatment was presented by Summerlin & Baring (2012) using Monte Carlo simulations, who showed the importance of the mean magnetic field orientation in the DSA process as well as the effect of MHD turbulence in determining the post-shock spectral index. Analytical estimates of the spectral index for parallel relativistic shocks (Kirk et al. 2000; Keshet & Waxman 2005) and for perpendicular shocks (Takamoto & Kirk 2015) have also shown remarkable consistency with the results from Monte Carlo simulations.

For our hybrid framework, modeling the post-shock spectral distribution using the Monte Carlo method (Summerlin & Baring 2012) is computationally very expensive and beyond the scope of the present work. Instead we adopt analytical estimates to account for DSA in the test particle limit valid for highly turbulent relativistic shocks. The slope of the spectral distribution associated with each macro-particle will depend on the compression ratio of the shock, r, and the angle Θ_B between the shock normal and magnetic field vector. To estimate these quantities, we have devised a strategy based on a shock detection algorithm and the corresponding change in the energy distribution of the particle as it crosses the shock. This is based on the following steps.
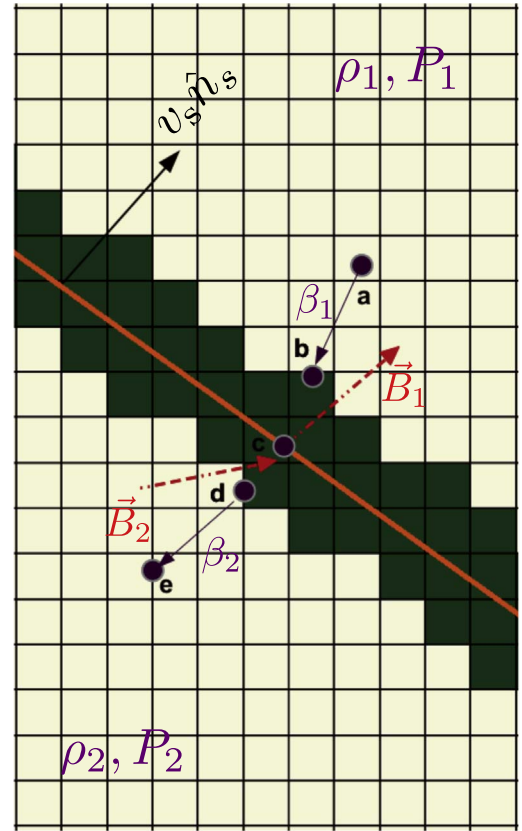

Figure 1. Different positions of the particle and corresponding diagnostics.

1. We first flag computational zones lying inside a shock when the divergence of the fluid velocity is negative, i.e., $\nabla \cdot \boldsymbol{v} < 0$ and the gradient of thermal pressure is above a certain threshold, ϵ_{sh} (see also the Appendix of Mignone et al. 2012). Typically we observe that a value $\epsilon_{\mathrm{sh}} \sim 3$ is enough to detect strong shocks. Shocked zones are shaded in green in Figure 1.

2. Away from shocked zones (point a in Figure 1), the particle spectral distribution evolves normally following the method outlined in the previous section.

3. When the macro-particle enters a flagged zone (point b in Figure 1), we start to keep track of the fluid state (such as density, velocity, magnetic field, and pressure) by properly interpolating them at the macro-particle position.

4. As the particle travels across the shocked area (points b, c, and d), we compute the maximum and minimum values of thermal pressure. The pre-shock fluid state $\boldsymbol{U}_1$ is then chosen to correspond to that with minimum pressure and, likewise, the post-shock state $\boldsymbol{U}_2$ to that with maximum pressure.

5. As the macro-particle leaves the shock (point d), the pre- and post-shock states $\boldsymbol{U}_1$ and $\boldsymbol{U}_2$ are used to compute the orientation of the shock normal $\hat{\boldsymbol{n}}_s$ and thereafter the shock speed. We employ the co-planarity theorem, stating that the magnetic fields on both sides of shock front, $\boldsymbol{B}_1$ and $\boldsymbol{B}_2$, lie in the same plane as the shock normal, $\hat{\boldsymbol{n}}_s$. Furthermore, the jumps in velocity and magnetic field across the shock must also be co-planar with the shock plane (Schwartz 1998). By knowing two vectors co-planar to the plane of the shock, we can easily

obtain $\hat{\boldsymbol{n}}_s$ through their cross product:

$$
\hat{\boldsymbol{n}}_s = \begin{cases} \pm \dfrac{\boldsymbol{\beta}_2^{\mathrm{arb}} - \boldsymbol{\beta}_1^{\mathrm{arb}}}{|\boldsymbol{\beta}_2^{\mathrm{arb}} - \boldsymbol{\beta}_1^{\mathrm{arb}}|} & \text{if } \theta^{\mathrm{arb}} \approx 0° \text{ or } 90° \\[2ex] \pm \dfrac{(\boldsymbol{B}_1 \times \Delta\boldsymbol{\beta}^{\mathrm{arb}}) \times \Delta\boldsymbol{B}}{|(\boldsymbol{B}_1 \times \Delta\boldsymbol{\beta}^{\mathrm{arb}}) \times \Delta\boldsymbol{B}|} & \text{otherwise} \end{cases} \tag{26}
$$

where, $\boldsymbol{\beta}_{1,2}^{\mathrm{arb}}$ is the velocity vector in the pre- and post-shock states for an arbitrary frame (here the rest frame of underlying fluid) and θ^{arb} is the angle between the magnetic field and the shock normal in that frame. The jumps in the fluid quantities are denoted by Δ, so that $\Delta\boldsymbol{B} = \boldsymbol{B}_2 - \boldsymbol{B}_1$ and $\Delta\boldsymbol{\beta}^{\mathrm{arb}} = \boldsymbol{\beta}_2 - \boldsymbol{\beta}_1$. Special care has to be taken to estimate the shock normal in the case of parallel and perpendicular shocks as the jump across the B field in the fluid rest frame will be zero (i.e., $\Delta\boldsymbol{B} = 0$).

We then compute the shock speed by imposing conservation of mass flux across the shock:

$$
\rho_1 \gamma_1 (\boldsymbol{\beta}_1 - v_{\mathrm{sh}} \hat{\boldsymbol{n}}_s) \cdot \hat{\boldsymbol{n}}_s = \rho_2 \gamma_2 (\boldsymbol{\beta}_2 - v_{\mathrm{sh}} \hat{\boldsymbol{n}}_s) \cdot \hat{\boldsymbol{n}}_s \tag{27}
$$

where the pre- and post-shock values are evaluated in the lab frame. The previous equation holds also in the non-relativistic case by setting the Lorentz factors to unity.

6. Next we compute the shock compression ratio r defined as the ratio of upstream and downstream velocities in the shock rest frame (β'_1 and β'_2, respectively):

$$
r = \frac{\boldsymbol{\beta}_1' \cdot \hat{\boldsymbol{n}}_s}{\boldsymbol{\beta}_2' \cdot \hat{\boldsymbol{n}}_s}. \tag{28}
$$

In the the non-relativistic case, the shock rest frame can be trivially obtained using a Galilean transformation. In this case, the compression ratio can also be obtained from the ratio of densities across the shock (see Equation (87)). However, this is no longer true in the case of relativistic shocks. The reference frame transformation is not trivial in this case and multiple rest frames are possible. In our approach, we transform from the lab frame to the *normal incidence frame* (NIF; see Appendix B) to obtain the compression ratio using Equation (89).

7. The compression ratio r and the orientation Θ_B of the magnetic field $\boldsymbol{B}$ with respect to the shock normal $\hat{\boldsymbol{n}}_s$ in the shock rest frame are used to update the particle distribution $\chi_{\mathrm{p}}(E, t^d)$ in the post-shock region. In particular, we inject a power-law spectrum in the post-shock region following $\mathcal{N}_{\mathrm{p}}(E, t^d) = \mathcal{N}(\epsilon_0)(E/\epsilon_0)^{-q+2}$ where ϵ_0 is the lower limit of the injected spectra and $\mathcal{N}(\epsilon_0)$ is the normalization constant. These two quantities depends on two user-defined parameters, namely the ratio of non-thermal to thermal (real) particle densities, δ_n, and the ratio of total energy of the injected real particles to the fluid internal energy density, δ_e (see e.g., Mimica et al. 2009; Böttcher & Dermer 2010; Fromm et al. 2016). In our recipe, we reset the particle energy distribution to the predicted DSA power law by also taking into account the pre-existing population. Therefore, we solve

$$
\tilde{\mathcal{A}}(\epsilon_0) \int_{\gamma_0}^{\gamma_1} \left(\frac{\gamma}{\gamma_0}\right)^{-q+2} d\gamma = \delta_n \frac{\rho}{m_{\mathrm{i}}} + n^{\mathrm{old}} \tag{29}
$$

and

$$
\tilde{\mathcal{A}}(\epsilon_0) \int_{\gamma_0}^{\gamma_1} \left(\frac{\gamma}{\gamma_0}\right)^{-q+2} \gamma d\gamma = \frac{\delta_e \mathcal{E}}{m_{\mathrm{e}} c^2} + \frac{E^{\mathrm{old}}}{m_{\mathrm{e}} c^2} \tag{30}
$$

to obtain the value of $\tilde{\mathcal{A}}(\epsilon_0)$ and $\epsilon_0 = \gamma_0 m_{\mathrm{e}} c^2$. The number density n^{old} and energy E^{old} are obtained by integrating the spectra of the macro-particle before it has entered the shock. In Equation (29), ρ is the value of fluid density interpolated at the macro-particle's position and m_{i} is the ion mass (we assume the thermal fluid density is dominated by protons). $\mathcal{E}$ is the fluid internal energy density interpolated at the particle position. Finally, the high-energy cut-off, ϵ_1, is estimated using the balance of synchrotron timescale, τ_{sync}, to the acceleration timescale τ_{acc} (Böttcher & Dermer 2010; Mimica & Aloy 2012).

$$
\gamma_1 = \frac{\epsilon_1}{m_{\mathrm{e}} c^2} = \left(\frac{9 c^4 m_e^2}{8 \pi B \lambda_{\mathrm{eff}} e^3}\right)^{1/2} \tag{31}
$$

where m_e is the electron mass while the acceleration efficiency λ_{eff} is derived from the acceleration timescale as given by Takamoto & Kirk (2015):

$$
\lambda_{\mathrm{eff}} = \frac{\eta r}{\beta_1'^2 (r - 1)} \left[\cos^2 \Theta_{B1} + \frac{\sin^2 \Theta_{B1}}{1 + \eta^2} \right. \\ \left. + \frac{r B_1'}{B_2'} \left(\cos^2 \Theta_{B2} + \frac{\sin^2 \Theta_{B2}}{1 + \eta^2} \right) \right] \tag{32}
$$

where the dimensionless free parameter $\eta > 1$ is the ratio of gyro-frequency to scattering frequency and chosen to be a constant. Primed quantities are computed in the shock rest frame. The angles Θ_{B1} and Θ_{B2} represent the angles between the magnetic field vector and the shock normal in the upstream and downstream region. We treat shocks as quasi-parallel when $\eta \cos \Theta_{B2} \geqslant 1$ and quasi-perpendicular otherwise (see Sironi & Spitkovsky 2009).

8. The upper energy cutoff may exceed the maximum allowed energy imposed by the Larmor radius constraint (see Equation (25)). If this is the case, we reset γ_1 to γ_L^{cf} in order to avoid spatial spreading of micro-particles.

9. As the macro-particle approach developed here aims to study large observable scales, micro-physical aspects of the DSA including amplification of magnetic fields and turbulent scattering have to be treated at the sub-grid level. The free (dimensionless) parameter η encapsulates the micro-physical nature of electron scattering associated with shock acceleration. Studies of quasi-perpendicular relativistic shocks have shown small-angle scattering to be the dominant mechanism (Kirk & Reville 2010; Sironi et al. 2013) for accelerating electrons, particularly in relativistic shocks. In this regime, η is a function of energy: $\eta \propto E$. Here, for simplicity, we adopt a constant value of η for both the downstream and the upstream flows. This may overestimate the acceleration efficiency particularly in the quasi-perpendicular case (see Equation (31)).

10. The power-law index, q, for non-relativistic shocks used in our model is that obtained from the steady state theory of DSA (Drury 1983),

$$
q = q_{\mathrm{NR}} = \frac{3r}{r - 1}. \tag{33}
$$

In case of relativistic shocks, q is obtained using analytical estimates from Keshet & Waxman (2005), particularly under the assumption of isotropic diffusion,

$$q = \frac{3\beta_1' - 2\beta_1'\beta_2'^2 + \beta_2'^3}{\beta_1' - \beta_2'} = q_{\mathrm{NR}} + \left(\frac{1 - 2r}{r - 1}\right)\beta_2'^2 \quad (34)$$

where β_1' and β_2' are the upstream and downstream velocity components along the shock normal in the NIF. In our test-particle framework, we assume isotropic diffusion for values of $\eta \cos \Theta_{B2} \geqslant 1$ and use the spectral index from Equation (34), while for more oblique shocks we adopt the analytic estimate obtained by Takamoto & Kirk (2015) for perpendicular shocks,

$$q = q_{\mathrm{NR}} + \frac{9}{20} \frac{r + 1}{r(r - 1)} \eta^2 \beta_1'^2. \quad (35)$$

11. Once the particle has left the shock (point e in Figure 1, the distribution function is again updated regularly as explained in Section 2.3.2.

3. Emission and Polarization Signatures

In the previous sections, we described the framework and the methods used for following the temporal evolution of the distribution function of the ensemble of NTPs attached to each Lagrangian macro-particle. Knowledge of the distribution function allows us to compute the non-thermal radiation emitted by each macro-particle and from the spatial distribution of macro-particles we can reconstruct the spatial distribution of non-thermal radiation. The non-thermal processes that we will consider are synchrotron and IC emission on a given radiation field and we will then be able to obtain intensity and polarization maps for each temporal snapshot. We now describe synchrotron emission, while Section 3.2 will be devoted to IC radiation.

3.1. Synchrotron Emission

The synchrotron emissivity, in the direction $\hat{\boldsymbol{n}}'$, per unit frequency and unit solid angle, by an ensemble of ultra-relativistic particles is given by (see Ginzburg & Syrovatskii 1965):

$$J_{\mathrm{syn}}'(\nu', \hat{\boldsymbol{n}}') = \int \mathcal{P}'(\nu', E', \psi') N'(E', \hat{\boldsymbol{\tau}}') dE' d\Omega_\tau' \quad (36)$$

where all primed quantities are evaluated in the local co-moving frame, which has a velocity $\boldsymbol{\beta} = \boldsymbol{v}/c$ with respect to the observer. Here, $\mathcal{P}'(\nu', E', \psi')$ is the spectral power per unit frequency and unit solid angle emitted by a single ultra-relativistic particle, with energy E', and whose velocity makes an angle ψ' with the direction $\hat{\boldsymbol{n}}'$, while $N'(E', \hat{\boldsymbol{\tau}}') dE' d\Omega_\tau'$ represents the number of particles with energy between E' and $E' + dE'$ and whose velocity is inside the solid angle $d\Omega_\tau'$ around the direction $\hat{\boldsymbol{\tau}}'$. In performing the integrals, we can take into account that the particle radiative power in the ultra-relativistic regime is strongly concentrated around the particle velocity and therefore only the particles with velocity along $\hat{\boldsymbol{n}}'$ contribute to the integral; we can then set $N'(E', \hat{\boldsymbol{\tau}}') = N'(E', \hat{\boldsymbol{n}}')$. Inserting in Equation (36) the expression for $\mathcal{P}$, which can be found in Ginzburg & Syrovatskii (1965), we then

get

$$J_{\mathrm{syn}}'(\nu', \hat{\boldsymbol{n}}_{\mathrm{los}}', \boldsymbol{B}') = \frac{\sqrt{3}\,e^3}{4\pi m_e c^2} |\boldsymbol{B}' \times \hat{\boldsymbol{n}}_{\mathrm{los}}'| \int_{E_i}^{E_f} \mathcal{N}'(E') F(x) dE' \quad (37)$$

where the direction taken by $\hat{\boldsymbol{n}}_{\mathrm{los}}'$ is the direction of the line of sight, we assume that the radiating particles are electrons, and we take a particle distribution that is isotropic and covers an energy range between a minimum energy E_i and a maximum energy E_f. From the isotropic condition we can also write

$$\mathcal{N}'(E') = 4\pi N'(E', \hat{\boldsymbol{n}}'). \quad (38)$$

Finally, the function $F(x)$ is the usual Bessel function integral given by

$$F(x) = x \int_x^\infty K_{5/3}(z) dz \quad (39)$$

where the variable x is

$$x = \frac{\nu'}{\nu_{cr}'} = \frac{4\pi m_e^3 c^5 \nu'}{3 e E'^2 |\boldsymbol{B}' \times \hat{\boldsymbol{n}}_{\mathrm{los}}'|} \quad (40)$$

and ν_{cr}' is the critical frequency at which the function $F(x)$ peaks. Similarly, the linearly polarized emissivity is given by

$$J_{\mathrm{pol}}'(\nu', \hat{\boldsymbol{n}}_{\mathrm{los}}', \boldsymbol{B}') = \frac{\sqrt{3}\,e^3}{4\pi m_e c^2} |\boldsymbol{B}' \times \hat{\boldsymbol{n}}_{\mathrm{los}}'| \int_{E_i}^{E_f} \mathcal{N}'(E') G(x) dE' \quad (41)$$

where the Bessel function $G(x) = x K_{2/3}(x)$.

Equations (37) and (41) give the emissivities in the co-moving frame as functions of quantities measured in the same frame; we need, however, the emissivities in the observer frame as functions of quantities in the same frame. These can be obtained by applying the appropriated transformations:

$$J_{\mathrm{syn}}(\nu, \hat{\boldsymbol{n}}_{\mathrm{los}}, \boldsymbol{B}) = \mathcal{D}^2 J_{\mathrm{syn}}'(\nu', \hat{\boldsymbol{n}}_{\mathrm{los}}', \boldsymbol{B}'), \quad (42)$$

$$J_{\mathrm{pol}}(\nu, \hat{\boldsymbol{n}}_{\mathrm{los}}, \boldsymbol{B}) = \mathcal{D}^2 J_{\mathrm{pol}}'(\nu', \hat{\boldsymbol{n}}_{\mathrm{los}}', \boldsymbol{B}') \quad (43)$$

where the Doppler factor $\mathcal{D}$ is given by

$$\mathcal{D}(\boldsymbol{\beta}, \hat{\boldsymbol{n}}_{\mathrm{los}}) = \frac{1}{\gamma(1 - \boldsymbol{\beta} \cdot \hat{\boldsymbol{n}}_{\mathrm{los}})}, \quad (44)$$

γ is the bulk Lorentz factor of the macro-particle, and ν', $\hat{\boldsymbol{n}}_{\mathrm{los}}'$, and $\boldsymbol{B}'$ can be expressed as functions of ν, $\hat{\boldsymbol{n}}_{\mathrm{los}}$, and $\boldsymbol{B}$ through the following expressions:

$$\nu' = \frac{1}{\mathcal{D}} \nu \quad (45)$$

$$\hat{\boldsymbol{n}}_{\mathrm{los}}' = \mathcal{D}\left[\hat{\boldsymbol{n}}_{\mathrm{los}} + \left(\frac{\gamma^2}{\gamma + 1}\boldsymbol{\beta} \cdot \hat{\boldsymbol{n}}_{\mathrm{los}} - \gamma\right)\boldsymbol{\beta}\right] \quad (46)$$

$$\boldsymbol{B}' = \frac{1}{\gamma}\left[\boldsymbol{B} + \frac{\gamma^2}{\gamma + 1}(\boldsymbol{\beta} \cdot \boldsymbol{B})\boldsymbol{\beta}\right]. \quad (47)$$

Using Equations (42) and (43), we can get for each macro-particle the associated total and polarized emissivities, at any time. The values are then *deposited* from the macro-particle on to the grid cells so as to give grid distributions of total and polarized emissivities, $\mathcal{J}_{\mathrm{syn}}(\nu, \hat{\boldsymbol{n}}_{\mathrm{los}}, \boldsymbol{r})$ and $\mathcal{J}_{\mathrm{pol}}(\nu, \hat{\boldsymbol{n}}_{\mathrm{los}}, \boldsymbol{r})$, as functions of the position $\boldsymbol{r}$.

Specific intensity maps can now be obtained by integrating the synchrotron emissivity, $\mathcal{J}_{\mathrm{syn}}(\nu, \boldsymbol{r})$ along the line of sight, in the direction $\hat{\boldsymbol{n}}_{\mathrm{los}}$,

$$I_{\nu}(\nu, X, Y) = \int_{-\infty}^{\infty} \mathcal{J}_{\mathrm{syn}}(\nu, X, Y, Z) dZ, \qquad (48)$$

where we introduced a Cartesian observer's frame where the axis Z is taken along the line of sight and the axes X and Y are taken in the plane of the sky. The total intensity represents the first Stokes parameter. To compute the other Stokes parameters, Q_{ν} and U_{ν} (neglecting circular polarization), we need to estimate the polarization angle, χ. Such an estimate would require us to account for proper relativistic effects like position angle swings (Lyutikov et al. 2003; Del Zanna et al. 2006). The two Stokes parameters in the plane of the sky are given by (see Del Zanna et al. 2006)

$$Q_{\nu}(\nu, X, Y) = \int_{-\infty}^{\infty} \mathcal{J}_{\mathrm{pol}}(\nu, X, Y, Z) \cos 2\chi \, dZ \qquad (49)$$

$$U_{\nu}(\nu, X, Y) = \int_{-\infty}^{\infty} \mathcal{J}_{\mathrm{pol}}(\nu, X, Y, Z) \sin 2\chi \, dZ \qquad (50)$$

where

$$\cos(2\chi) = \frac{q_X^2 - q_Y^2}{q_X^2 + q_Y^2}, \qquad \sin(2\chi) = -\frac{2 q_X q_Y}{q_X^2 + q_Y^2} \qquad (51)$$

and

$$q_X = (1 - \beta_Z) B_X - \beta_X B_Z, \qquad q_Y = (1 - \beta_Z) B_Y - \beta_Y B_Z \qquad (52)$$

and the polarization degree is

$$\Pi = \frac{\sqrt{Q_{\nu}^2 + U_{\nu}^2}}{I_{\nu}}. \qquad (53)$$

3.2. IC Emission

The other important emission mechanism that we consider is the IC effect due to the interaction of relativistic electrons with a given radiation field. In the present work, we will focus on the IC emission on seed photons due to the isotropic CMB radiation.

The co-moving IC photon emissivity $\dot{n}_{\mathrm{IC}}'(\nu', \hat{\boldsymbol{n}}') = j_{\mathrm{IC}}'/h\nu'$ (number of photons per frequency interval per unit solid angle around the direction $\boldsymbol{n}'$) is given by

$$\dot{n}_{\mathrm{IC}}'(\nu', \hat{\boldsymbol{n}}') = \int_0^{\infty} d\varepsilon_{\mathrm{ph}}' \int d\Omega_{\mathrm{ph}}' \int dE' \int d\Omega_{\tau}'$$
$$N(E', \boldsymbol{\tau}) \, c(1 - \boldsymbol{\beta}_e \cdot \boldsymbol{l}') n_{\mathrm{ph}}'(\varepsilon_{\mathrm{ph}}', \boldsymbol{l}') \sigma(\varepsilon_{\mathrm{ph}}', \boldsymbol{l}', \nu', \hat{\boldsymbol{n}}') \qquad (54)$$

where $n_{\mathrm{ph}}'(\varepsilon_{\mathrm{ph}}', \boldsymbol{l}')$ and $N'(E', \boldsymbol{\tau})$ are, respectively, the spectral density distribution of the seed photons, in the co-moving frame, as a function of photon energy $\varepsilon_{\mathrm{ph}}'$ and photon direction $\boldsymbol{l}'$, and the electron distribution as a function again of energy E' and direction $\boldsymbol{\tau}$. The factor $c(1 - \boldsymbol{\beta}_e \cdot \boldsymbol{l}')$ arises from the differential velocity between the photon and the electron, and $\boldsymbol{\beta}_e$ is the scattering electron velocity vector in units of c. The scattering cross section, σ, depends, in principle, on the directions and energies of incident and outgoing photons.

The seed photons are the CMB photons; then in the observer frame they have a blackbody distribution with energy density

$$u_{\mathrm{CMB}} = 4 \frac{\sigma_B}{c} [T_{\mathrm{CMB}}(1 + z)]^4 \qquad (55)$$

where σ_B is the Stefan–Boltzmann constant, $T_{\mathrm{CMB}} = 2.728\mathrm{K}$ is the CMB temperature, and z is the redshift of the source we study. We approximate the blackbody distribution with a monochromatic distribution with energy equal to the peak energy of the blackbody, $\varepsilon_{\mathrm{CMB}} = k_B T_{\mathrm{CMB}}$, where k_B is the Boltzmann constant. If the flow moves at relativistic bulk speed ($\gamma \gg 1$), the seed photons in the co-moving frame are bunched in the direction opposite to the macro-particle velocity. The photon spectral energy distribution can be written as

$$n_{\mathrm{ph}}'(\varepsilon_{\mathrm{ph}}', \boldsymbol{l}') = \frac{\gamma u_{\mathrm{CMB}}}{\varepsilon_{\mathrm{CMB}}} \delta(\boldsymbol{l}' - \hat{\boldsymbol{\beta}}) \delta(\varepsilon_{\mathrm{ph}}' \varepsilon_{\mathrm{CMB}}), \qquad (56)$$

where $\hat{\boldsymbol{\beta}}$ is the unit vector in the direction of the macro-particle velocity and δ represents the Dirac function. The electron distribution is assumed to be isotropic $N'(E', \boldsymbol{\tau}) = \mathcal{N}'(E')/4\pi$

The scattered photons are beamed along the direction of the scattering electron so that $\hat{\boldsymbol{n}}' = \boldsymbol{\tau}$ and emerge after scattering with average final energy

$$h\nu' \approx \left(\frac{E'}{m_e c^2} \right)^2 \varepsilon_{\mathrm{ph}}'(1 + \boldsymbol{\tau}' \cdot \hat{\boldsymbol{\beta}}). \qquad (57)$$

Using the Thomson cross section, which is justified when the incident photon energy in the electron frame is much less than the electron rest mass energy, i.e., assuming $\sigma(\varepsilon_{\mathrm{ph}}', \boldsymbol{l}', \nu', \hat{\boldsymbol{n}}') = \sigma_{\mathrm{T}}$, inserting Equations (55)–(57) in Equation (54) and taking into account the appropriate Lorentz transformations, we can finally express the IC emissivity in the observer frame for each macro-particle as

$$J_{\mathrm{IC}}(\nu, \hat{\boldsymbol{n}}_{\mathrm{los}}) = \left(\frac{\mathcal{D}^2 m_e c^2}{2\pi k_B} \right) \sigma_B \sigma_{\mathrm{T}} T_{\mathrm{CMB}}^3 (1 + z)^3$$
$$(\mathcal{D}\Lambda\chi)^{1/2} \mathcal{N}\left(\sqrt{\frac{\chi}{\mathcal{D}\Lambda}} \right), \qquad (58)$$

where $\mathcal{D}$ is the Doppler factor,

$$\Lambda = \frac{1 + \hat{\boldsymbol{n}}_{\mathrm{los}} \cdot \hat{\boldsymbol{\beta}}}{1 + \beta} \qquad (59)$$

and

$$\chi = \frac{h\nu}{k_B T_{\mathrm{CMB}}(1 + z)}. \qquad (60)$$

As we do for the synchrotron emissivity, we can deposit the IC emissivity on to the grid cells so as to give the grid distribution of $\mathcal{J}_{\mathrm{IC}}(\nu, \hat{\boldsymbol{n}}_{\mathrm{los}}, \boldsymbol{r})$ and finally we can obtain specific intensity maps by integrating along the line of sight.

4. Numerical Benchmarks

In this section we report a suite of numerical benchmarks aimed at validating the correctness of our numerical implementation.

4.1. Classical Planar Shock

In the first test problem we assess the accuracy of our method in verifying that the shock properties (such as
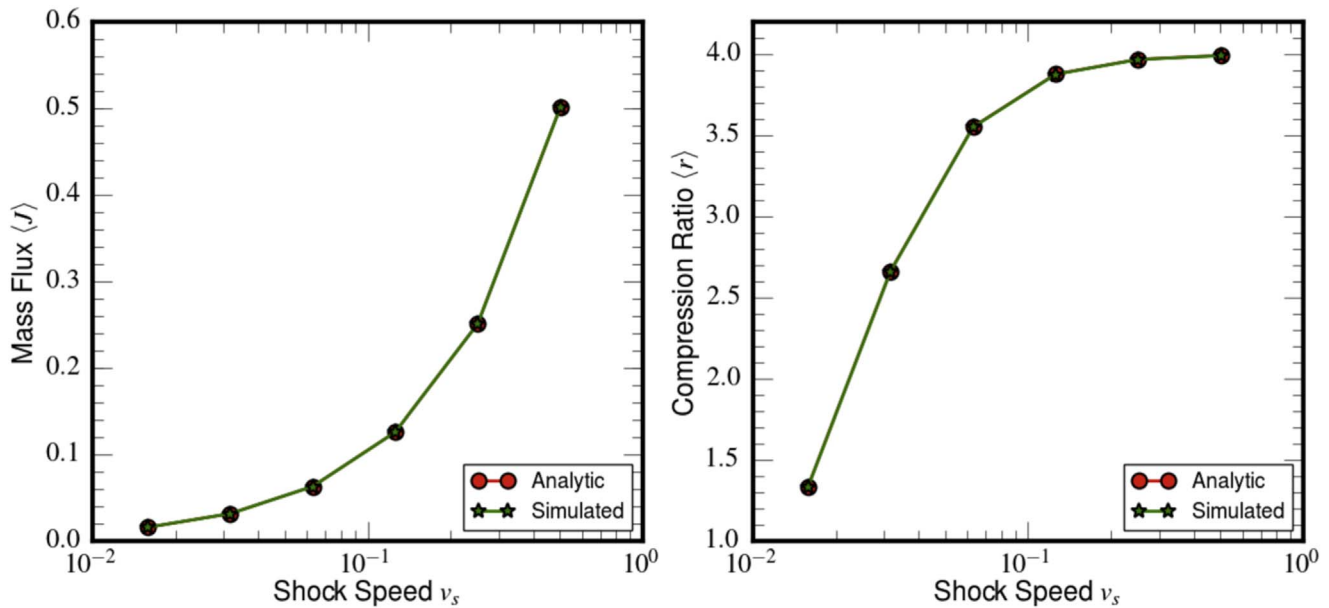
Figure 2. Analytical (red dots) and simulated (green stars) values of the mass flux in the shock rest frame J (left panel) and compression ratio r (right panel) for the classical MHD planar shock test with $\theta_B = 30°$.

compression ratio, mass flux, etc.), are sampled correctly as macro-particles cross the discontinuity.

We solve the classical MHD equation with an ideal equation of state ($\Gamma = 5/3$) on the Cartesian box $x \in [0,4]$, $y \in [0,2]$ using a uniform resolution of 512×256 grid zones. The initial condition consists of a planar shock wave initially located at $x_s(0) = 1$ and moving to the right with speed $v_{\rm sh}$. We work in the upstream reference frame where the gas is at rest with density and pressure equal to $\rho_1 = 1$, $p_1 = 10^{-4}$. Here the magnetic field lies in the $x - y$ plane and it is given by $\boldsymbol{B} = B_1(\cos\theta_B, \sin\theta_B)$ where $\theta_B = 30°$ is the angle formed by $\boldsymbol{B}$ and the x axis while B_1 is computed from the plasma beta, $\beta_{p1} = 2p_1/B_1^2 = 10^2$. The downstream state is computed by explicitly solving the MHD jump conditions once the upstream state and the shock speed $v_{\rm sh}$ are known. Zero-gradient boundary conditions are set on all sides. We place a total of $N_p = 16$ macro-particles in the region $1.5 < x < 3$ in the pre-shock medium and perform six different runs by varying the shock speed $v_{\rm sh} \in [0.01, 1]$ on a logarithmic scale.

While crossing the shock, fluid quantities are interpolated at each macro-particle position following the guidelines described in Section 2.4. From these values we compute, for each macro-particle, the mass flux J_p and the compression ratio r_p in the shock rest frame. As all macro-particles experience the same shock, we compute the average value

$$\langle J \rangle = \frac{1}{N_{\rm p}} \sum_{\rm p} J_{\rm p} \qquad (61)$$

and similarly for the compression ratio $\langle r \rangle$. In the left and right panels of Figure 2 we compare, respectively, $\langle J \rangle$ and $\langle r \rangle$ with the analytical values obtained from the computations at different shock velocities. Our results are in excellent agreement with the analytic values, thereby demonstrating the accuracy of steps (i)–(vi) of the algorithm described in Section 2.4 in the non-relativistic case.

4.2. Relativistic Planar Shock

Next, we extend the previous problem to the relativistic regime with the aim of further describing the spectral evolution of macro-particles as they cross the discontinuity. The initial conditions are similar to the previous test case but the upstream medium has now a transverse velocity $\beta = 0.01\hat{y}$ and the magnetic field has a different strength given by $\beta_{p1} = 0.01$. We solve the relativistic MHD equation with the Taub (1948)/ Mathews (1971) equation of state and repeat the computation considering different values of the shock speed $v_{\rm sh}$. As in the classical case, we introduce $N_p = 16$ macro-particles in the upstream reference frame in the region $1.5 < x < 3$.

As explained in Section 2.4, we estimate relevant quantities such as the mass flux J and compression ratio r by transforming to the NIF where the upstream velocity is normal to the shock front. The strategy used for frame transformation is more involved than its classical counterpart and is illustrated in Appendix B.

The left panel of Figure 3 shows the analytical mass flux J in the lab frame (see Equation (27)) as red dots and the average value of the mass flux $\langle J \rangle$ obtained from the particles in the NIF frame as green stars. A good agreement between the analytical and numerical results highlights the accuracy of our method in sampling the shock and the subsequent frame transformation required to quantify the compression ratio. A comparison between the analytical values (red dots) for the compression ratio r with that obtained from macro-particles (green stars) is shown in the right panel of Figure 3. We observe that the average compression ratio, $\langle r \rangle$, estimated as the ratio of upstream and downstream velocities in NIF using macro-particles, agrees with analytical values for varying shocks speeds. The compression ratio value approaches $r = 4.0$ for smaller shock speeds, as expected from the non-relativistic limit.

Next we focus on the evolution of the spectral energy distribution and, to this purpose, appropriate physical scales must be introduced. We set the unit length scale $L_0 = 10^2$ pc and the speed of light as the reference velocity, i.e., $V_0 = c$.
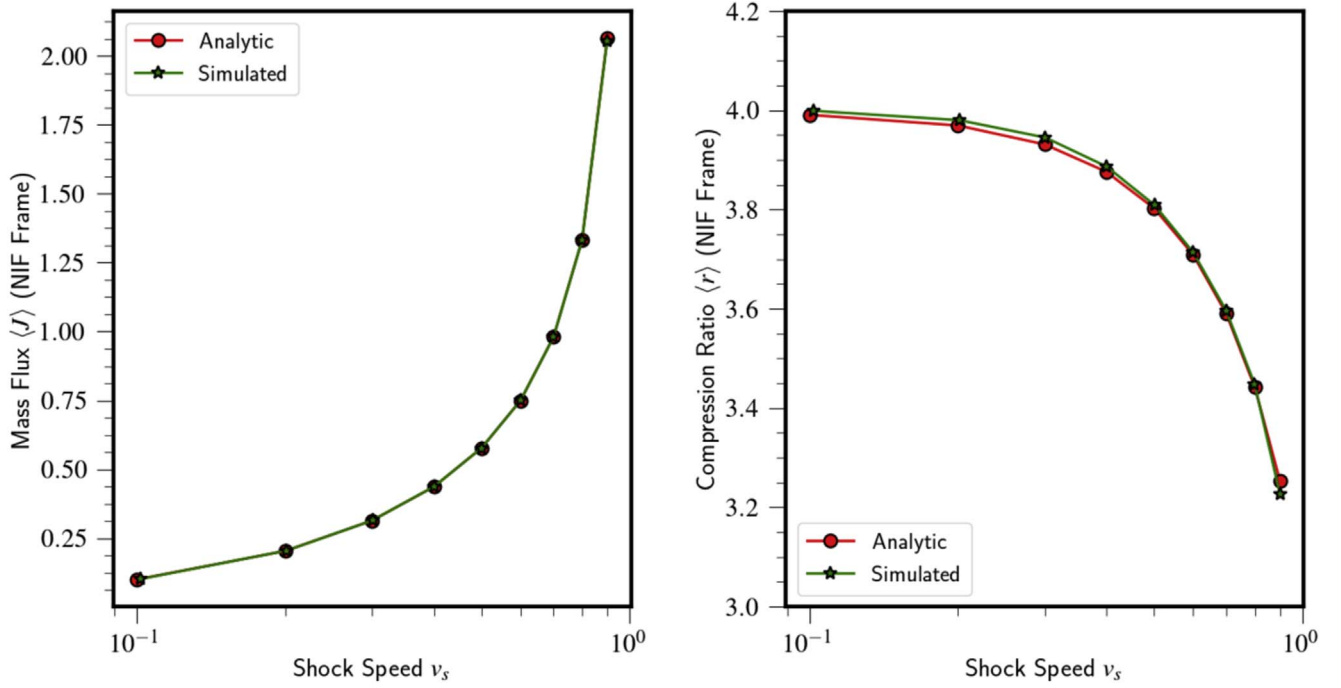
Figure 3. Left panel : comparison of mass flux and compression ratio for the relativistic planar shock case with $\Theta_B = 3.0$. Analytical mass flux J in the lab frame (or NIF) estimated from Equation (27) is shown as red dots, whereas its average value $\langle J \rangle$ obtained from macro-particles is shown as green stars. In the right panel, the analytical (red dots) and simulated values of compression ratio r (green stars) estimated using Equation (89) are shown. The simulated values are obtained as macro-particles traverse the relativistic planar shock and the sampled quantities across the shock are transformed to a shock rest frame.

The energy distribution for each macro-particle is initialized as a power law with $m = 9$ (see Equation (24)) with the initial number density of real particles $\mathcal{N}_{tot} = 10^{-4}$ cm^{-3}.

The initial spectral energy ranges from $E_{min} = 0.63$ MeV to $E_{max} = 0.63$ TeV, with $n_E = 500$ bins. The initial bounds are chosen to cover an observed frequency range from the radio band to X-rays for the chosen magnetic field strengths. The energy bounds of the spectral distribution as the macro-particles cross the shock are estimated from Equations (29) and (30) with $\delta_n = 0.9$ and $\delta_e = 0.5$.

We consider both quasi-parallel and quasi-perpendicular shocks where the angles between the shock normal and magnetic field vector are $\theta_B = 3°$ and $\theta_B = 83°$, respectively. The shock jump conditions are set to obtain a compression ratio $r \sim 3.6$ for both cases corresponding to the shock speed $v_s = 0.7c$. The density map and magnetic field orientation at $t = 0.98$ kyr are shown in the top panels of Figure 4 for the two cases.

The spectral evolution of a representative macro-particle is shown in the bottom panel of Figure 4 for the quasi-parallel (left) and quasi-perpendicular (right) cases. For the quasi-parallel case, the initial spectrum steepens at high energies in the presence of losses due to synchrotron emission. At time $t \sim 0.46$ kyr the macro-particle crosses the shock from the upstream region and the distribution function flattens its slope, yielding a spectral index $q = 4.15$ as estimated from Equation (34). Due to the large acceleration timescale for the quasi-parallel case, a high-energy cutoff $E_{max} \sim 6.25 \times 10^5$ GeV is obtained as indicated by the light blue curve in the left panel. This sudden change in the spectra can be attributed to steady-state DSA, whereby the spectrum is modified completely based on the compression ratio at the shock and particle density injected at the shock (see Equations (29)

and (30)). Subsequently, the high-energy part cools down due to synchrotron emission, reaching an energy of $\sim 10^4$ GeV (red curve). In the case of a quasi-perpendicular shock, we obtain a steeper distribution owing to the dependence of the spectral index ($q = 6.2$) on η^2 (Equation (35)). Also, the high-energy cutoff lessens due to the inefficiency of quasi-perpendicular shocks in accelerating particles to high energy. The subsequent evolution of the particle spectrum is then governed by radiation losses due to synchrotron and IC cooling and leads to a similar steepening at high energies. This test clearly shows the validity of our method in estimating the compression ratio r and the change in the spectral slope under the DSA approximation.

4.3. Relativistic Magnetized Spherical Blast Wave

In the next test case, we test our numerical approach on curved shock fronts to assess the accuracy of the method in the case where shock propagation is not grid-aligned.

The initial conditions consist of a relativistic magnetized blast wave centered at the origin with density and pressure given by

$$(\rho, p) = \begin{cases} (1, 1) & \text{for} \quad R < 0.8l_0 \\ (10^{-2}, 3 \times 10^{-5}) & \text{otherwise} \end{cases} \quad (62)$$

where $R = \sqrt{x^2 + y^2}$ and l_0 is the scale length. The magnetic field is perpendicular to the plane, $\boldsymbol{B} = B_0\hat{z}$, with $B_0 = 10^{-6}$ and an ideal equation of state with adiabatic index $\Gamma = 5/3$ is used.

For symmetry reasons, we consider only one quadrant using 512^2 computational zones on a square Cartesian domain of side $6l_0$. Reflecting conditions are applied at $x = y = 0$ while outflow boundaries hold elsewhere. The HLL Riemann solver, linear interpolation, and a second-order Runge–Kutta scheme
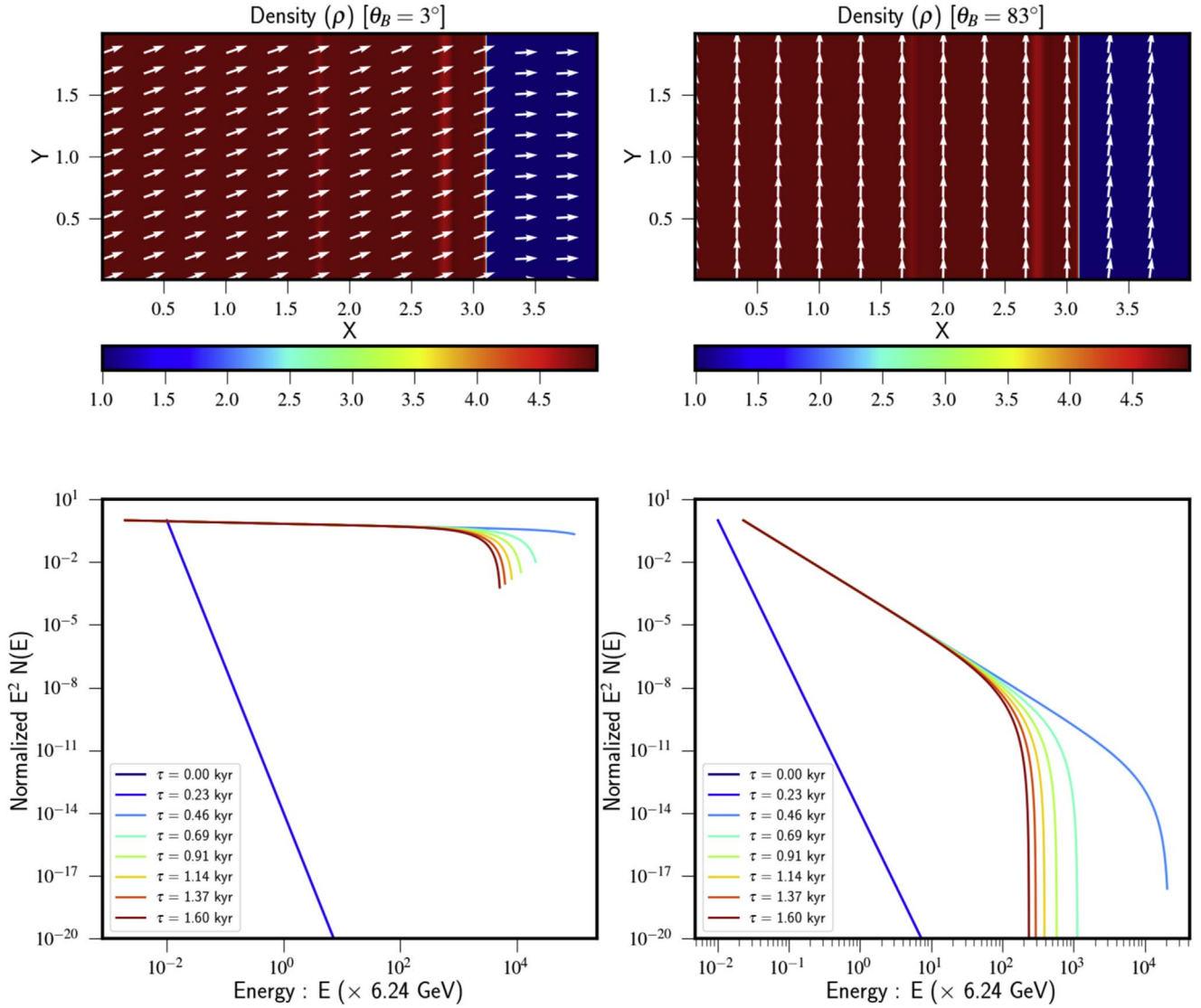
Figure 4. Top panels: density distribution in color at time $t = 0.98$ kyr along with magnetic field vectors shown as white arrows for the quasi-parallel case $\theta_B = 3°$ (left) and quasi-perpendicular case $\theta_B = 83°$ (right) for the relativistic planar shock test. Bottom panels: the corresponding evolution of normalized spectral distribution of a representative macro-particle.

are used to evolve the fluid. We employ 360 macro-particles uniformly distributed between $0 < \phi < \pi/2$ and placed at the cylindrical radius $R_p = \sqrt{x_p^2 + y_p^2} = 2l_0$. Associated with each macro-particle is an initial power-law spectrum with index $m = 9$ covering an energy range of 10 orders of magnitude with 500 logarithmically spaced uniform bins.

The over-pressurized regions develop a forward moving cylindrical shock that propagates along the radial direction. The shock velocity v_{sh} computed by different macro-particles (see Section 2.4) is shown in the top panel of Figure 5 as a function of the angular position and compared to a semi-analytical value $v_{sh} \approx 0.885$ obtained from a highly resolved 1D simulation. The numerical estimate of the shock speeds is consistent with the semi-analytical value within 1% relative error. Additionally, its value remains the same independently of the angular position of the macro-particle. This clearly demonstrates the accuracy of our hybrid shock tracking method for a curvilinear shock.

This shock speed is then used to perform a Lorentz transformation to the NIF in order to obtain the compression ratio, shown in the middle panel of Figure 5, from

macro-particles initially lying at different angles. Similar to the shock velocity estimate, the compression ratio also agrees very well with the semi-analytical estimate $r \approx 2.473$, shown as a red dashed line.

The bottom panel of Figure 5 shows the relative error in the estimate of mass flux, J_{NIF}, in the NIF. This is estimated as

$$\Delta J_{NIF}[\%] = 100 \left(\frac{J_{NIF} - J_{NIF}^{ref}}{J_{NIF}^{ref}} \right), \qquad (63)$$

where J_{NIF} is estimated from quantities interpolated on the macro-particles from the fluid. The reference value, J_{NIF}^{ref}, is estimated using the semi-analytical shock velocity and quantities across the shock from a highly resolved 1D simulation. The colors represent the value of the compression ratio.

4.4. Sedov–Taylor Explosion

In the next test we verify the accuracy of our method in computing the radiative loss terms by focusing on the adiabatic expansion term alone, for which an analytical solution is
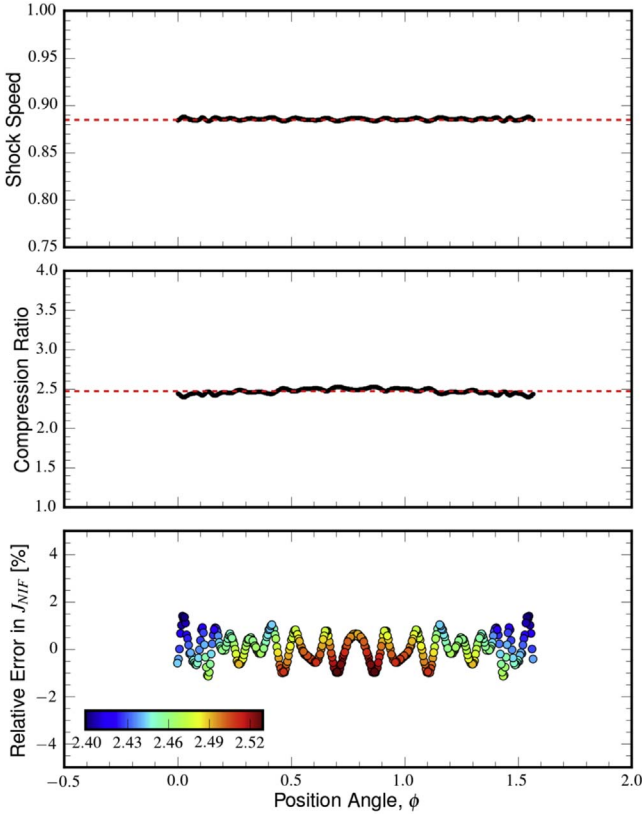
Figure 5. Variation of shock properties with angular position for the RMHD blast wave test. The shock velocity obtained from a single representative macro-particle is shown as black circles and the semi-analytical estimate from a very high resolution 1D run is shown as a red dashed line in the top panel. The middle panel shows the variation of compression ratio obtained from the particles. The relative error in the estimate of mass flux, J_{NIF}, in the normal incidence frame is shown in the bottom panel; the colors here indicate the value of compression ratio.

available. The fluid consists of a pure hydrodynamical ($B = 0$) Sedov–Taylor explosion in 2D Cartesian coordinates (x, y) on the unit square [0,1] discretized with 512^2 grid points. Density is initially constant $\rho = 1$. A circular region around the origin ($x = 0$, $y = 0$) with an area $\Delta A = \pi (\Delta r)^2$ is initialized with a high internal energy (or pressure), where $\Delta r = 3.5/512$, while the region outside this circle has a lower internal energy (or pressure). Using an ideal equation of state with adiabatic index 5/3 we have,

$$\rho e = \begin{cases} \dfrac{E}{\Delta A} & \text{for } r \leqslant \Delta r \\ 1.5 \times 10^{-5} & \text{otherwise} \end{cases} \qquad (64)$$

where $r = \sqrt{x^2 + y^2}$ and input energy $E = 1.0$. Therefore we have a contrast of $\approx 4.54 \times 10^8$ in ρe.

For this test problem we have used the standard HLL Reimann solver with Courant number CFL = 0.4. Reflective boundary conditions are set around the axis while open boundary conditions are imposed elsewhere.

Using the dimensional analysis, the *self-similar* solution for the Sedov–Taylor blast can be derived. In terms of the scaled radial co-ordinate $\eta \equiv r(Et^2/\rho)^{-1/5}$, the shock location is

obtained by

$$r_s(t) = \eta_s \left(\frac{Et^2}{\rho} \right)^{1/5} \propto t^{2/5}. \qquad (65)$$

where η_s is a constant of the order of unity, t is the time in *arbitary* units and r is the spherical radius. The shock velocity follows via time differentiation as

$$v_{\text{sh}}(t) = \frac{dr_s}{dt} = \frac{2}{5} \frac{r_s(t)}{t} \propto t^{-3/5}. \qquad (66)$$

Due to the self-similar nature, we can further relate the flow velocity at any spherical radius r to that of the shock velocity obtained from Equation (66):

$$v(r, t) \equiv \frac{v_{\text{sh}}(t)}{r_s(t)} r \equiv \frac{2}{5} r t^{-1}. \qquad (67)$$

Thus, we have $\nabla \cdot \boldsymbol{v} \propto t^{-1}$. To estimate the evolution of spectral energy for a single macro-particle due to adiabatic expansion we have to solve Equation (14)

$$E(t) = E_0 \exp \left(-\int_{t_0}^{t} c_a(t) dt \right) \qquad (68)$$

where $c_a(t) = \frac{1}{3} \nabla \cdot \boldsymbol{v} \propto t^{-1}$. Plugging Equation (68) into Equation (19) gives the temporal dependence of an initial power-law spectral density $\mathcal{N}(E, t)$:

$$\mathcal{N}(E, t) \propto E^{-m} \left(\frac{t_0}{t} \right)^{m+2} \propto E_0^{-m} \left(\frac{t_0}{t} \right)^2, \qquad (69)$$

a result already known by Kardashev (1962).

In order to compare the above analytical result with simulations, we initialize a total of 1024 macro-particles that are placed uniformly within the domain of unit square. Each particle is initialized with a power-law spectrum $\chi_p^0 \propto E^{-m}$ (see Equation (24)) with $m = 3$ covering a range of six orders of magnitude in the actual particle energy with a total of 250 equally spaced logarithmic energy bins. As the aim of this test is to study solely the effects due to adiabatic expansion, we switch off (by hand) the impact of shock acceleration due to the forward moving spherical shock.

Equation (69) indicates that the ratio of spectral density varies with the inverse square law of time and does not affect the initial distribution slope m. This implies that losses due to adiabatic expansion modify all energy bins in the same way and the resulting spectral evolution involves a parallel shift of the spectrum. Such an evolution of the spectrum for a representative particle is shown in the right panel of Figure 6.

The particle distribution along with the fluid density (in color) at time $t = 0.85$ is shown in the left panel of Figure 6. The particles that were initially placed uniformly have expanded with the flow as expected from their Lagrangian description. Also, in the regions of high density just behind the shock, a large concentration of particles is seen. The spectral evolution of the particle marked in white is shown in the right panel. Radiation losses due to adiabatic cooling affect all energy bins uniformly and, as a result, the spectrum shifts toward the lower-energy side, keeping the same value of initial spectral power, i.e., $m = 3$. To test the accuracy of the
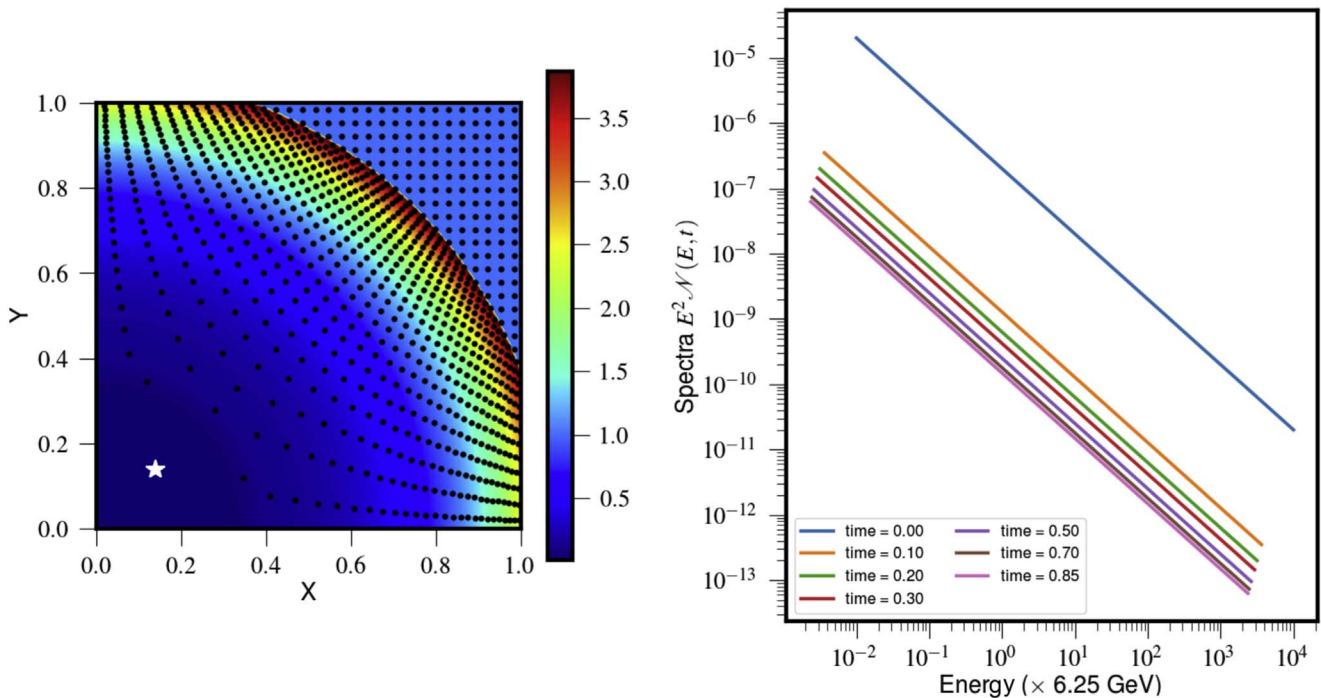
Figure 6. Left panel: particle distribution (black points) along with the fluid density (in color) for the Sedov–Taylor explosion test at time $t = 0.85$ (in arbitrary units) with a resolution of 512^2. Right panel: temporal spectral evolution for the macro-particle marked as a white star in the left panel.

numerical method applied, we have done a convergence study by varying the grid resolution of the unit square domain.

In the top panel of Figure 7, we compare the spectral distribution for a particular energy bin ($E = E_{\min}(t)$) of a single particle under consideration with the analytical solution described above. We observe that, for the run with 512^2 resolution, the simulated values are in perfect agreement with the analytical estimates. However, the errors in the estimate of the slope become as large as 10%–15% with low resolution. The bottom panel of Figure 7 shows the relative error in % for the estimate of the slope for different grid resolutions. The error is visibly large for grid resolutions <100 points. However, having more than 128 points in the domain results in reducing the error within the $\pm 2\%$ band as indicated by two black dashed lines, and the study is fully converged for runs with 512 grid points.

4.5. Relativistic Spherical Shell

In this test, we verify our numerical implementation to estimate synchrotron emissivities (Equations (42) and (43)) and the polarization degree from Stokes parameters (Equations (49) and (50)), specifically testing the changes due to relativistic effects.

4.5.1. Co-moving Frame

We initialize a magnetized sphere in a 3D square domain of size $L = 40$ pc. The sphere has a constant density ($\rho_0 = 1.66 \times 10^{-25}$ g cm^{-3}) and pressure ($P_0 = 1.5 \times 10^{-4}$ dyne cm^{-2}), is centered at the origin, and has a radius of $R_s = 10$ pc. The three components of the velocity are given such that

$$\boldsymbol{v} = \beta \frac{R}{R_s}\{\sin(\theta)\cos(\phi),\ \sin(\theta)\cos(\phi),\ \cos(\theta)\} \qquad (70)$$
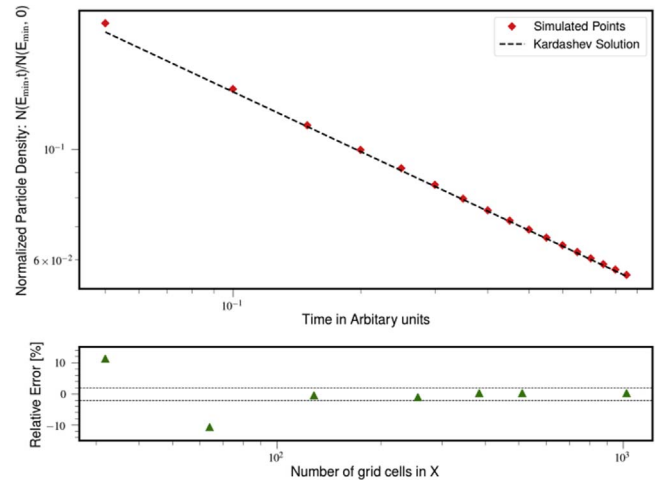

Figure 7. Top: comparison of the evolution with time (in arbitrary units) of a normalized spectral distribution, $\mathcal{N}(E_{\min}, t)$ (red squares) with an analytical solution obtained from Equation (69) (black dashed line). Bottom: results from the convergence study with different resolution. The green triangles represent the relative errors (%) in estimating the analytical slope for the variation of $\mathcal{N}(E_{\min}, t)$ with respect to time. The two black dashed lines mark the $\pm 2\%$ error.

where $\beta = \sqrt{1 - 1/\gamma^2}$ with bulk Lorentz factor γ and R, θ and ϕ are spherical co-ordinates expressed using Cartesian components.

The Cartesian components of the purely toroidal magnetic fields are set as

$$B_x = -B_0 \sin(\phi)\sqrt{x^2 + y^2}$$
$$B_y = B_0 \cos(\phi)\sqrt{x^2 + y^2}$$
$$B_z = 0.0 \qquad (71)$$

where $B_0 \sim 60$ mG is the magnitude of magnetic field vector.

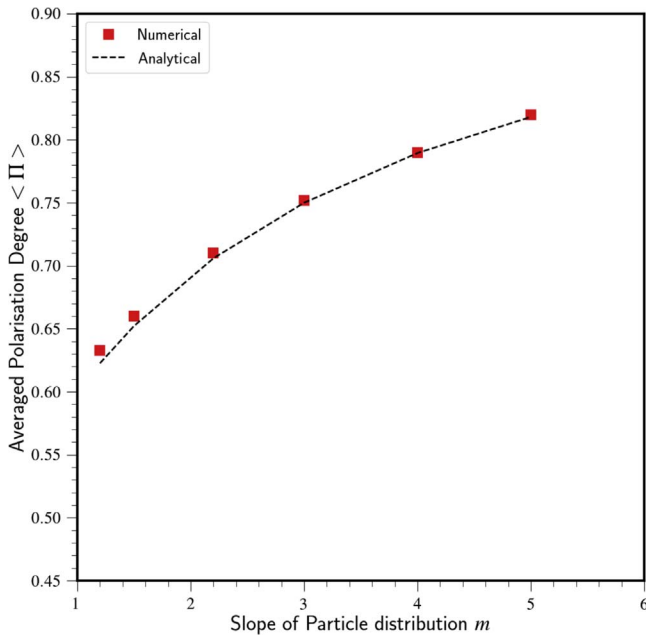**Figure 8.** Comparison of the numerically estimated averaged ratio of $J_{sy}(\nu)$ with $J_{pol}(\nu)$ for $\nu = 10^{10}$ GHz (red squares) with the theoretical values obtained from Equation (72) shown as the black dashed line.

A total of 100 macro-particles with an initial power-law spectral distribution are randomly placed on the shell of width $0.1R_s$. For each particle, the spectral range from $E_{min} = 10^{-8}$ erg to $E_{max} = 10^2$ erg is sampled by a total of 250 logarithmically spaced energy bins. The synchrotron emissivity, $J_{sy}(\nu)$ and linearly polarized emissivity $J_{pol}(\nu)$ from each macro-particle are estimated numerically using Equations (42) and (43) for an observed frequency $\nu = 10^{10}$ GHz with the initial power-law spectral distribution. Their ratio gives a value of polarization fraction Π_i, for ith macro-particle. We compute the arithmetic average of numerically estimated polarization degree and this is denoted by $\langle \Pi \rangle$

In the co-moving frame, the theoretical value expected for the polarization degree on the shell is simply given by (e.g., Longair 1994)

$$\Pi = \frac{m + 1}{m + 7/3}. \qquad (72)$$

In figure Figure 8, we have compared the numerical averaged value (in co-moving frame) for different initial power-law spectral slopes m with the above theoretical estimate (Equation (72)).

4.5.2. Observer Frame

To obtain the polarization degree, Π_{obs} in the observer frame, the Stokes parameters given by Equations (49) and (50) have to be computed along with the polarization angle χ. Relativistic effects like position angle swing must be taken into account in order to calculate χ (e.g., Lyutikov et al. 2003; Del Zanna et al. 2006). Due to the relativistic motion, the emission is boosted, resulting in a rotation of linear polarization angle in the $\hat{n} - v$ plane. Though the value of fractional polarization is the same, the rotation of polarization angle is different for different elements of the emitting object. These relativistic kinematic effects can therefore result in the maximum observed polarization being smaller than the theoretical

upper limit given by Equation (72). This crucial ingredient has been implemented in our hybrid framework to compute the Stokes parameters and thereby the corrected fractional polarization in case of macro-particles moving in a relativistic flow. Here, we verify our numerical implementation by replicating the calculation of the averaged value of the Stokes parameters done by Lyutikov et al. (2003) for a quasi-spherical thin emitting shell.

In our case, an emitting element is represented by a macro-particle that is moving with the spherical shell with a velocity that depends on the two spherical co-ordinates θ and ϕ:

$$v = \beta \{\sin\theta \cos\phi, \sin\theta \cos\phi, \cos\theta\}, \qquad (73)$$

where β is a related to the Lorentz factor γ. The observer is in the x–z plane with

$$\hat{n} = \{\sin\theta_{obs}, 0, \cos\theta_{obs}\} \qquad (74)$$

as the unit vector along the line of sight and θ_{obs} is the angle with respect to the vertical z-axis. The shell is magnetized with a field that lies along

$$\hat{B} = \{-\sin\Psi' \sin\phi, -\sin\Psi' \cos\phi, \cos\Psi'\} \qquad (75)$$

where Ψ' is the magnetic pitch angle. Macro-particles placed uniformly on this shell will emit synchrotron emission based on their initial power-law spectra governed by the index m (same for all macro-particles). The dependence of volume-averaged Stokes parameters obtained from our numerical implementation for two values of Lorentz factor $\gamma = 10$ (solid lines) and $\gamma = 50$ (dashed lines) of the shell and three values of initial power-law index (i.e., $m = 1, 2,$ and 3) of the emitting macro-particles is shown in Figure 9. The left panel is for a value of the magnetic pitch angle $\Psi' = 45°$ and the right panel is for a purely toroidal field $\Psi' = 90°$.

For the case of a purely toroidal magnetic field, we observe that the value of the polarization degree saturates for $\theta_{obs} > 1/\gamma$, consistent with the electromagnetic model proposed to explain large values of polarization reported in GRBs (Lyutikov et al. 2003). As expected, the polarization fraction saturates at a smaller θ_{obs} for $\gamma = 50$ as compared to runs with $\gamma = 10$. The asymptotic value $\Pi \approx 56\%$ obtained for $m = 3$ (blue) is less than the maximum upper limit of 75% (using Equation (72)), in agreement with the estimates by Lyutikov et al. (2003). The effect of depolarization is further enhanced if the magnetic field distribution is changed using the value of $\Phi' = 45°$ (left panel). In this case, the asymptotic value of the polarization degree for $m = 3$ is $\leqslant 30\%$. This clearly shows the vital role of (de)-polarization degree in determining the magnetic field structure in the flow.

5. Astrophysical Applications

In this section, we describe a couple of astrophysical applications of the hybrid framework.

5.1. Supernova Remnant SN1006

The first application is to study classical DSA and properties of non-thermal emission from a historical Type IA supernova remnant (SNR), SN1006. The numerical setup chosen for this problem is identical to that of Schneiter et al. (2010). We perform an axisymmetric MHD simulation with a numerical grid of physical size of 12 and 24 pc in the r- and z-directions, respectively. The grid has a spatial resolution of 1.56×10^{-2} pc.
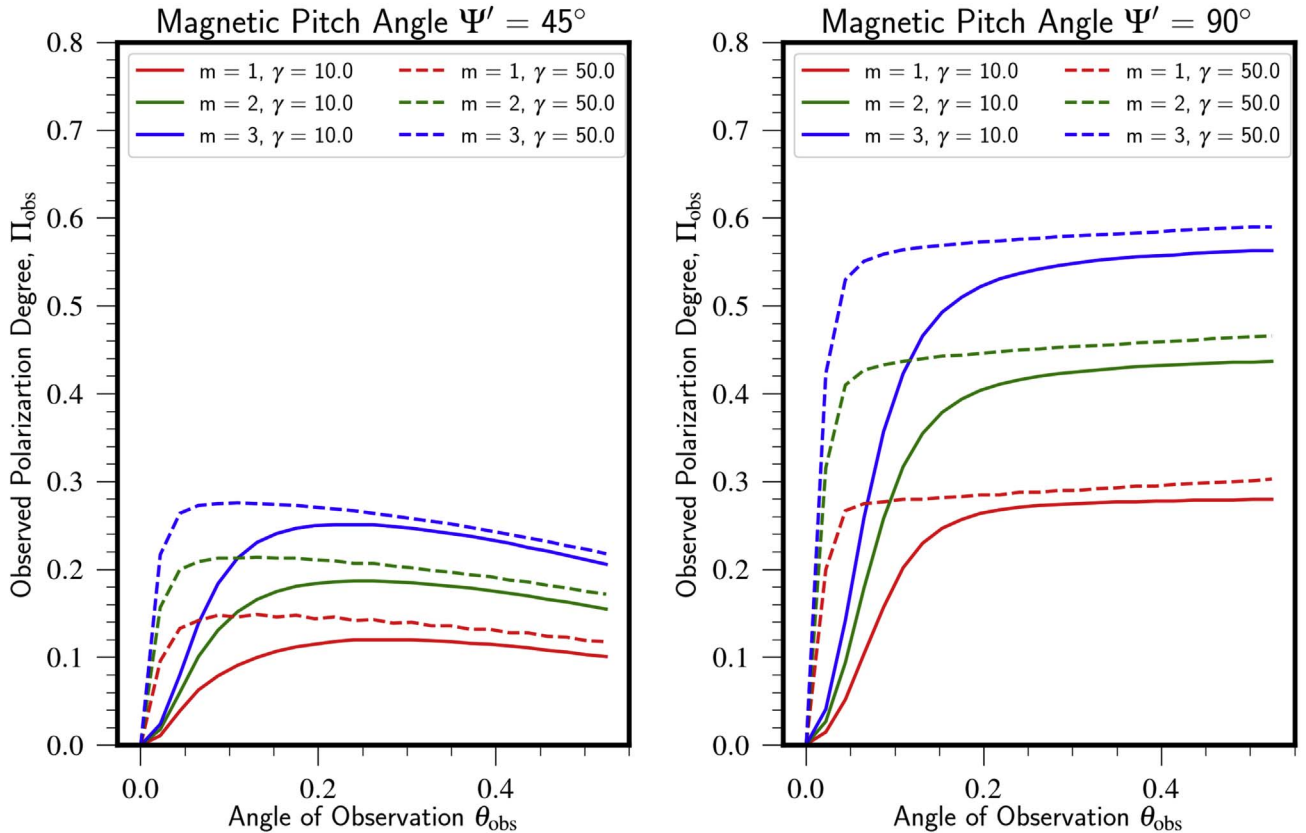
Figure 9. Left: dependence of observed polarization fraction Π_{obs} with observation angle θ_{obs} for a magnetic pitch $\Psi' = 45°$ and two values of Lorentz factor for the shell, $\gamma = 10$ (solid line) and 50 (dashed line). The distribution of macro-particles(radiating elements) is set to be a power law with three different spectral slopes, $m = 1$ (red), 2 (green) and 3 (blue). Right: same as the left panel but for a purely toroidal field ($\Psi' = 90°$).

The ambient interstellar medium has a constant number density, $n_{amb} = 0.05 \, cm^{-3}$. The initial magnetic field is chosen to be constant with a value of $2 \, \mu G$ and parallel to the z-axis. To numerically model the Type Ia SNR, we initialize a sphere with radius of 0.65 pc at the center of the domain such that it contains an ejecta mass of $1.4 M_\odot$. Within the sphere, the innermost region has a constant mass equivalent to $0.8 M_\odot$ while the rest of the mass is in the outer region. This outer region has an initial power-law density profile, $\rho \propto R_{sph}^{-7}$, where the spherical radius $R_{sph} = \sqrt{r^2 + z^2}$.

Figure 10 shows the fluid density for the SNR at time $\tau = 1008$ yr. The magnetic field is represented by red arrows. We see the formation of Rayleigh–Taylor instabilities at the contact wave. The forward spherical shock traverses the magnetic fields thereby modifying its vertical alignment. Due to compression from the shock, the magnetic flux just ahead of it is also enhanced and follows the curved shock as evident from the magnetic field vectors.

A total of 2.5×10^4 macro-particles are randomly initialized in the ambient medium. To each of them we attach a scalar quantity "color" whose value is initially set to be -2. However, as the simulation progresses in time, these macro-particles enter the shock and sample the compression ratio as described in Section 2.4. The scalar "color" for each macro-particle is then replaced by the value of the compression ratio of the shock it experiences. This helps to separate the particle population for further diagnostics. The initial population of particles (e.g., electrons) has a steep power-law spectral distribution with an index $m = 3$ covering a range $E_{min} \approx 0.63$ MeV to

$E_{max} \approx 0.31$ TeV. The inital value of E_{max} is set in accordance with the Larmor radius constraint, ensuring that every single macro-particle consists of an initial energy distribution of micro-particles that are situated very nearby in physical space (within one grid cell). This initial spectral distribution is evolved accounting for radiation losses due to adiabatic, synchrotron, and IC effects.

The macro-particle distribution (as scalar "color") at time $\tau = 1008$ yr is shown in the left panel of Figure 11. This distribution shows that most of the macro-particles have a compression ratio close to 4.0, indicating a strong adiabatic shock. For all the macro-particles that are shocked, we estimate the spectral energy index m using the shock compression ratio. We assume *isotropic* injection whereby the spectral index depends solely on the compression ratio and is independent of the orientation of the magnetic field with respect to the shock normal (see Equation (33)). A histogram of the spectral energy index showing a distinct peak around $m \approx 2.05$ is shown in the middle panel of Figure 11. Due to the skewness in the distribution, an arithmetic average of spectral energy index gives a value $\langle m \rangle = 2.1$. This is equivalent to a spectral frequency index 0.55, a value slightly flatter as compared to the observed estimate of 0.6 at radio wavelengths. Note that the value of m obtained here is immediately after the particle has traversed the shock. However, the subsequent evolution in a magnetized environment will result in radiative losses due to adiabatic expansion and synchrotron and IC losses, which will effectively steepen the spectrum, especially at very high energies. The spectral evolution is shown in the right panel of
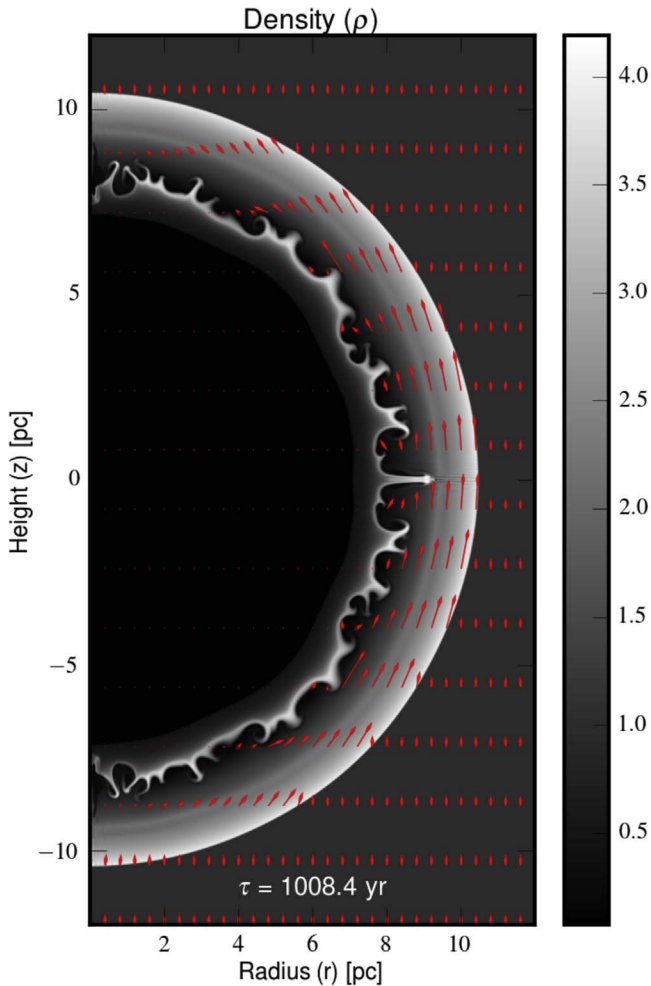
Density (ρ)

Figure 10. Evolution of fluid density at time $\tau \approx 1008$ yr along with magnetic field vectors, shown as red arrows.

Figure 11 for a representative single macro-particle. This macro-particle experiences the shock around 540 yr and its spectral energy distribution is flattened by the shock and also extended to higher energies. The rapid spectral change is, once again, caused by our "instantanous" steady state approach to DSA. The maximum energy obtained after the DSA is ≈16 TeV. Such an estimate is a factor 2.5 times smaller than the upper limit obtained by fitting the electron spectrum from SN1006 (Reynolds & Keohane 1999) assuming a magnetic field of 10 μG. As the shock passes, the losses due to adiabatic expansion are evident from a uniform downward shift over time. Losses due to synchrotron cooling are insignificant due to the cooling time being larger than the evolution time for electrons with few TeV energies for field strengths of the order of 10 μG in our simulations.

5.2. Shocks in Relativistic Slab Jets

The second application studies the particle acceleration at shocks in a two-dimensional relativistic slab jet.

The initial conditions consist of a Cartesian domain having a spatial extent of $(0, D = 10\pi a)$ and $(-D/2, D/2)$ along the x and y planes respectively. The domain is discretized with 384^2 grid cells. The slab jet is centered at $y = 0$ and has a vertical extent of length $a = 200$ pc on both sides of the central axis. The slab jet has a flow velocity given by a bulk Lorentz factor

$\gamma = 5$ along the x axis while the ambient medium is static. In order to avoid excitation of random perturbations due to the steep gradient in velocity at the interface we convolve the jet velocity with a smoothening function as described in Bodo et al. (1995). Additionally, a uniform magnetic field with a plasma $\beta = 10^3$ along the x axis corresponding to a field strength of ≈6 mG is introduced. As the main goal of this application is to model the interaction of under-dense AGN jets with the ambient, we choose a jet with a density ratio of $\eta = 10^{-2}$:

$$\frac{\rho(y, \eta)}{\rho_0} = \eta - (\eta - 1)\,\mathrm{sech}\left[\left(\frac{y}{a}\right)^6\right] \qquad (76)$$

where $\rho_0 = 10^{-4}$ cm^{-3} is the density of the jet on the central axis (i.e., $y = 0$). The jet is set to be in pressure equilibrium with the ambient, i.e., $P_{\mathrm{jet}} = P_{\mathrm{amb}} = 1.5 \times 10^{-9}$ dyne cm^{-2}. Periodic boundary conditions are imposed along the x axis and free boundary conditions are imposed at the top and bottom boundaries.

This initial configuration at time $\tau = 0$ is perturbed with a functional form that can excite a wide range of modes. We perturb the y component of the velocity using the antisymmetric perturbation described by Equation 2(b) of Bodo et al. (1995). The amplitude of the perturbation is chosen to be 1% of the initial bulk flow velocity. The wavelength of the fundamental mode is set equal to the size of the computational domain along the x direction; the corresponding wave number is $k_0 = 2\pi/D = 0.2/a$. These perturbations grow with time as a consequence of the Kelvin–Helmholtz instability, progressively steepen, and develop into shocks. These oblique shocks are typically seen in AGN jets as the bulk jet flow interacts with the surrounding ambient.

In order to study the effects of such shocks on the process of particle acceleration via DSA, we introduce two macro-particles per cell (~3×10^5 particles) at the initial time. The macro-particles are initialized with a very steep initial power-law spectrum ($m = 15$; see Equation (24)) covering a wide spectral energy range of eight orders of magnitude with $E_{\mathrm{min}} = 0.63$ keV to $E_{\mathrm{max}} = 63$ TeV with 250 bins. The initial number density of real particles is set to be $\mathcal{N}_0 = 10^{-4}\rho_0$. During the early stages of evolution when the shocks have yet to form, the particles experience radiative losses due to synchrotron and IC processes. After the perturbations steepen to form shocks, the particles are accelerated via DSA and their spectral distribution is modified as described in Section 2.4. The obliquity of magnetic field with respect to the shock normal is also accounted for in the estimate of the post-shock electron spectral slope q of the particle by using Equations (34) and (35). The free parameters used to determine the energy bounds of the shock modified spectral distribution are chosen as $\delta_n = 0.01$ and $\delta_e = 0.5$.

During the simulation run of 0.3 Myr, we record a total of 16,539 events when the spectral distribution of the macro-particles is altered on passing through the shock. The normalized probability distribution function (PDF) of the modified spectral slope q is shown in Figure 12. The PDF shows a reasonable spread in the shock-modified spectral slope q. We observe that the mean of the events of spectral modification results in a slope $\langle q \rangle \sim 3.1$ This spread arises due to our consistent approach of estimating the value of q based on the compression ratio of the shock and the obliquity
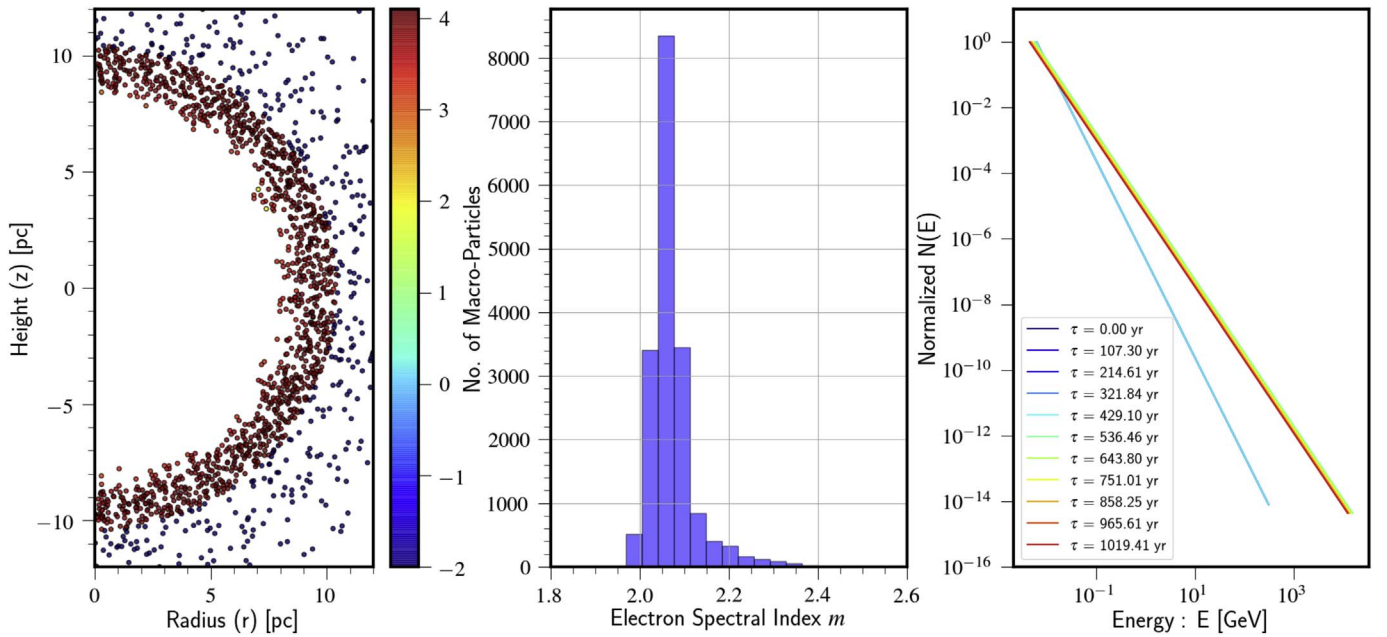
Figure 11. Left panel: particle distribution at time $\tau = 1008$ yr for the SN 1006 supernova remnant case. The colors represent the compression ratio due to shock while the negative values represent initial particles in the domain that have not interacted with the shock. Middle panel: histogram showing the electron spectral index m for all the particles that have been shocked. Right panel: evolution of spectral energy distribution for a single representative macro-particle.
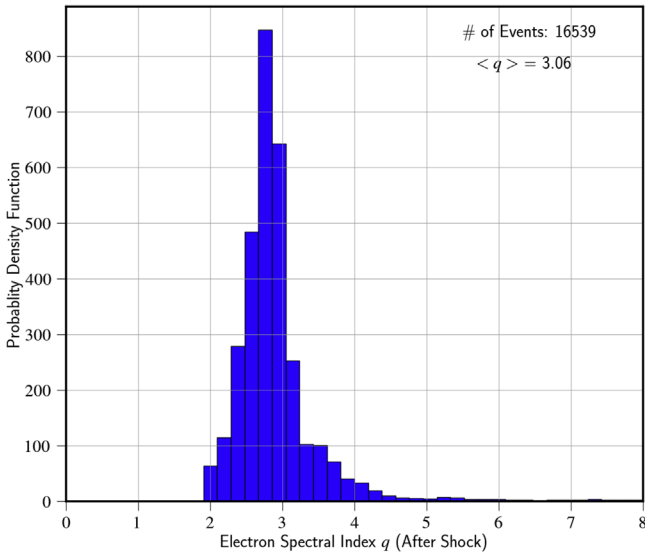

Figure 12. Normalized PDF of the modified spectral slope q as the particle crosses the shock during the evolution of the slab jet until 0.3 Myr.

of the magnetic field with respect to the shock normal. With our approach we relax the approximation of treating every shock as a strong shock with a fixed spectral slope of $q = 2.23$ (Mimica et al. 2009; Fromm et al. 2016) or $q = 2.0$ (de la Cita et al. 2016). The fixed choice of spectral index ($q \approx 2$) would result in an overestimate of the emissivity as the majority of shocks formed in our simulations have either lower strengths or are quasi-perpendicular, resulting in a steeper spectral distribution.

We estimate the synchrotron emissivity $\mathcal{J}_{\rm sy}(\nu, \hat{\boldsymbol{n}}_{\rm los}, \boldsymbol{r})$, fractional polarization Π (see Equations (42), (43)), and IC emissivity $\mathcal{J}_{\rm IC}(\nu, \hat{\boldsymbol{n}}_{\rm los}, \boldsymbol{r})$ (Equation (58)) using the instantaneous spectral distribution for each macro-particle. The above integral quantities for each macro-particle are then *deposited* onto the fluid grid. The line of sight is chosen to be $\theta_{\rm obs} = 20°$

with respect to the z-axis (pointing out of the plane). The Gaussian convoluted normalized emissivity (with standard deviation $\sigma_g = 9$) is shown in Figure 13 for three different observed frequencies at time $\tau \sim 0.14$ Myr. The left panel shows the emissivity at $\nu = 150$ MHz in the low-frequency radio band using spectral colors. The emissivity for 10 keV X-ray energy is shown in the middle panel and the IC emissivity at an energy of 0.5 MeV representing the soft-gamma band is shown in the right panel. In each of these panels, we also show the fluid density ρ in the background with copper colors. We observe a correlation between high-emissivity regions in the radio band with those of shocks formed as the jet interacts with the ambient medium. The X-ray emission at 10 keV is interesting and very distinct from that in the left and right panels. We observe X-ray emission as localized bright knots rather than a distributed emission in radio. The spots are associated with regions where there has been recent interactions of merging shocks as seen in the background fluid density. The weak emission features observed in the right panel in the soft-gamma band are correlated with those seen in the left panel. No localized bright spots are observed for the emission at 0.5 MeV. This can be understood from the fact that the same population of electrons responsible of the production of the low-frequency radio emission also up-scatter CMB photons ($T_{\rm CMB}(z) = 2.728$ K) to give rise to IC emission around the same energy band.

To better compare the distinct nature of radio and X-ray synchrotron emission, we overlap the normalized X-ray emission corresponding to an energy of 3 keV with normalized radio ($\nu = 15$ GHz) contours in the left panel of Figure 14. The X-ray emission is convoluted with a beam that is 1.5 times broader than that used to obtain the radio contours. Though our emissivity estimates from the slab jet are not integrated along the line of sight, we do see clear evidence of knotty emission in the X-ray bands that is offset from the radio peaks. The reason for this offset lies in the fact that they originate from different regions associated with the structure of oblique shocks. Radio
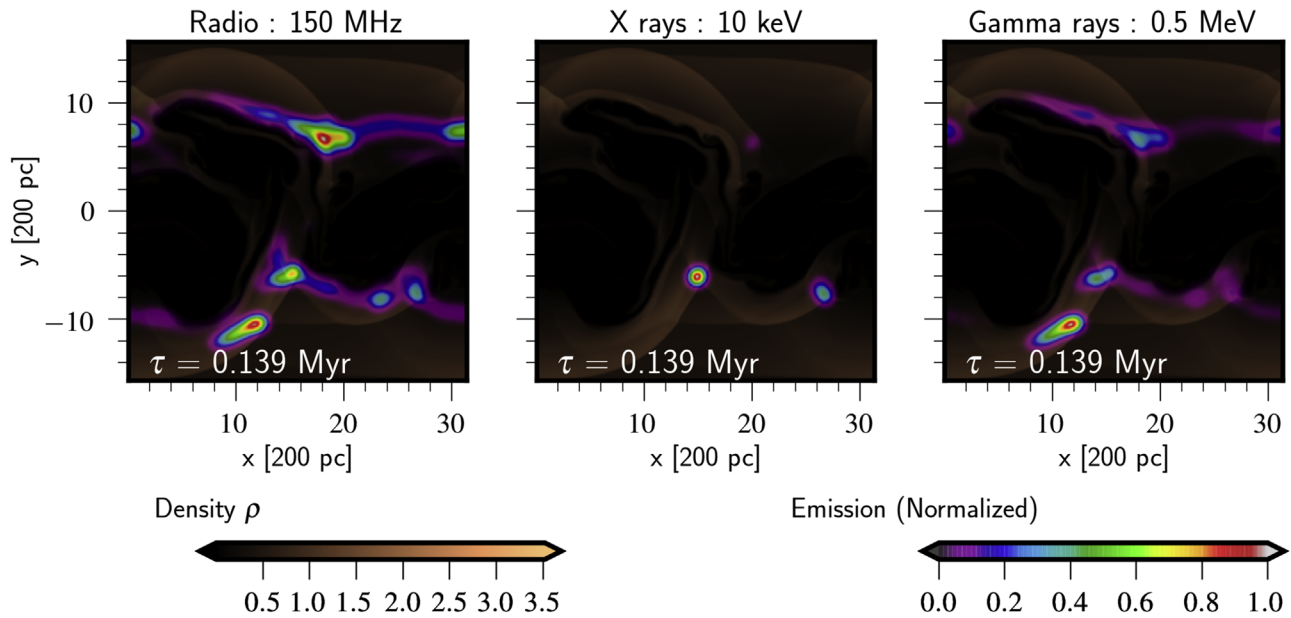
Figure 13. Multi-wavelength emission signatures from the slab jet simulation run at time $\tau = 0.137$ Myr. Each panel shows the fluid density ρ (as copper colors). The emissivities shown in each panel are obtained from instantaneous spectral distribution of particles and deposited on the grid. They are shown as spectral colors for three different observed frequencies, namely $\nu = 150$ MHz (left), 10 keV (middle) due to synchrotron processes, and 0.5 MeV (right) due to IC.

emission is mainly forming due to large-scale, long-lived shocks as the jet flow interacts with the ambient. Additionally, the radio electrons have a much longer synchrotron lifetime, allowing them to produce bright emission at low frequencies. As the large-scale, forward-moving shocks interact, they also result in the formation of reverse shocks, which eventually merge. Bright X-ray knots are produced where such a recent merging of reverse shocks takes place and are short-lived due to the very short synchrotron cooling time of high-energy electrons. Multi-wavelength observations of the kpc-scale jet in the powerful radio galaxy 3C 346 have shown signatures of an offset of about 0.8 kpc between the radio and X-ray emission (Worrall & Birkinshaw 2005; Dulwich et al. 2009). The synthetic emissivity map obtained from our simulations of oblique shocks is able to very well reproduce such offsets.

Additionally, the magnetic obliquity plays a crucial role in determining the spectral index and energy bounds of injected spectrum at shocks. The magnetic fields at oblique shocks typically become perpendicular to the jet flow, and therefore would result in a steeper spectral slope. This can been understood from the distribution of fractional polarization shown in the right panel of Figure 14. We have overlaid contours (spectral colors) of Π for radio band $\nu = 15$ GHz on the copper background of fluid density. The contour levels vary from 20% (black) to 70% (gray). Regions of high degree of polarization >50% are seen at the merging large-scale shocks, indicating strong polarization of synchrotron emission there. Multi-wavelength spectral studies of typical AGN jets like M87 and 3C 264 have shown evidence of X-ray synchrotron emission and harder spectral indices toward the edge of the jet (Perlman et al. 1999, 2010; Worrall & Birkinshaw 2005). A consequence of this is the presence of a high degree of polarization at the edges of the interface between the jet bulk flow and ambient medium. Optical and radio polarization studies in 3C 264 show a similar high degree > 45% close to the edges (e.g., Perlman et al. 2006, 2010).

Thus, our implementation of DSA at relativistic shocks for the case of slab jets shows similar qualitative features as

observed for typical AGN jets. A one-to-one comparison with observed flux estimates will be made in a subsequent paper using 3D RMHD jet simulations.

6. Discussion and Conclusion

We have presented a state-of-the-art hybrid framework for the PLUTO code which describes the spectral evolution of highly energetic particles by means of (mesh-less) Lagrangian macro-particles embedded in a classical or relativistic MHD fluid. The main purpose of this work is the inclusion of sub-grid micro-physical processes at macroscopic astrophysical scales where the fluid approximation is adequate. While the MHD equations are integrated by means of standard Godunov-type finite-volume schemes already available with the code, macro-particles obey the relativistic cosmic-ray transport equation in the diffusion approximation. Back-reaction from particle to the fluid is not included and will be considered in forthcoming works.

The main features that characterize our hybrid framework are summarized below.

1. Lagrangian macro-particles follow fluid streamlines and embody a collection of actual physical particles (typically electrons) with a finite distribution in energy space. For each macro-particle we solve, away from shocks, the cosmic ray transport equation in momentum (or energy space) to model radiation losses due to synchrotron, adiabatic expansion, and IC effects, based on local fluid conditions. The transport equation is solved semi-analytically using the method of characteristics to update the energy coordinates in a Lagrangian discretization.

2. In the presence of magnetized shocks, we have described a novel technique to account for particle energization due to DSA processes. This involves sampling the local fluid quantities (such as velocity, magnetic field, and pressure) in the upstream and downstream states to estimate the shock velocity along with the shock normal. These quantities are critical to performing the transformation to
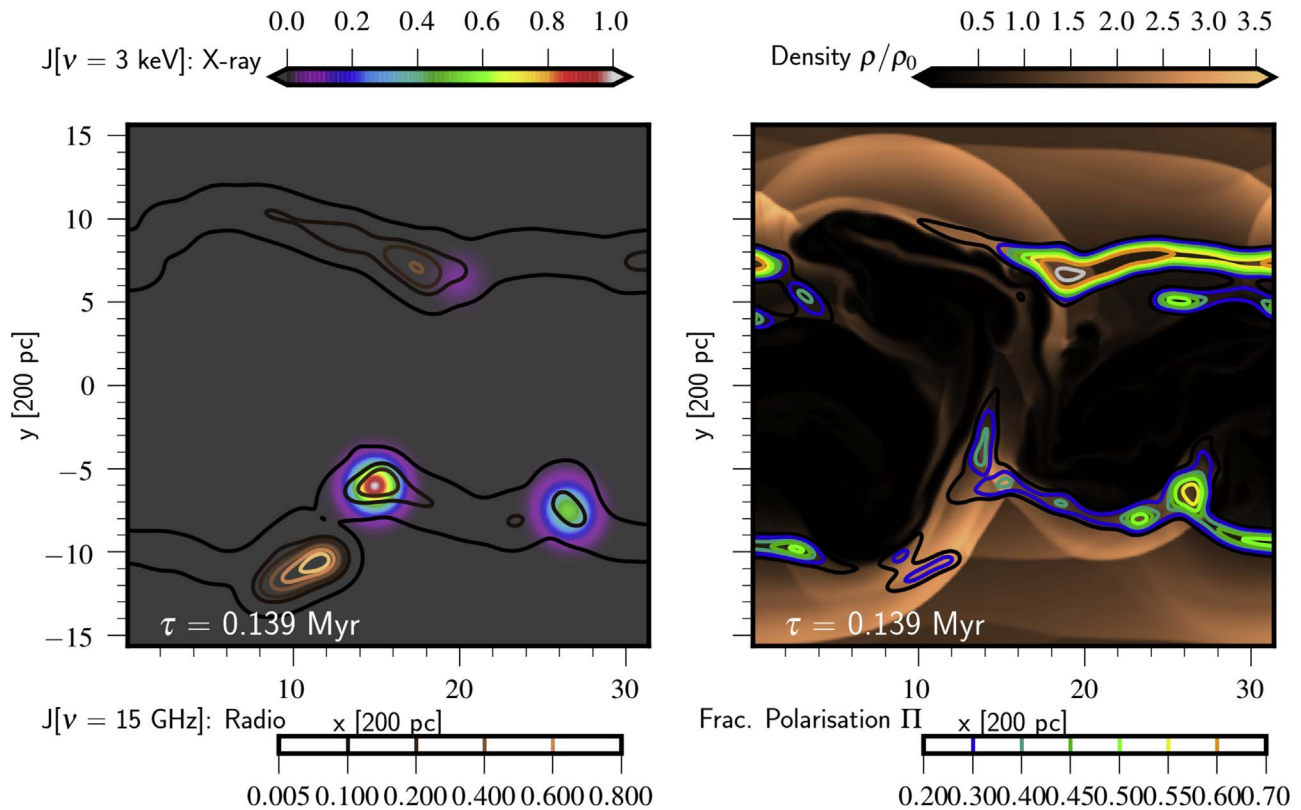
Figure 14. Multi-wavelength emissivity map of the slab jet at time $\tau = 0.137$ Myr (left panel). The color map shows the Gaussian-convoluted normalized X-ray (3 keV) emissivity and overlaid are the contours for Gaussian-convoluted normalized radio ($\nu = 15$ GHz) emissivity. The right panel shows the density of the flow in the copper color map at the same time and overlaid are the contours of the polarization degree whose values range from $\Pi = 20\%$ (black contours) to $\Pi = 70\%$ (gray contours).

the NIF where the compression ratio can then be calculated. We have verified the validity of our shock-detection scheme by comparing it with theoretical estimates from 2D planar shocks. The technique works also for curved as well as oblique shocks with very good accuracy.

Knowledge of the shock normal and of the local magnetic field direction enables us to include obliquity dependence in the estimate of the post-shock power-law index of the particle energy distribution. In this way our model is able to distinguish between quasi-parallel (more efficient) and quasi-perpendicular (less efficient) shocks, the latter resulting in a steeper spectrum and depending on the amount of parameterized (unresolved) turbulence. In both cases, the high-energy cut-off is estimated consistently from the acceleration timescale derived without assuming equipartition, but rather by considering particle diffusion along and across the magnetic field lines.

3. The spectral distribution from each macro-particle is then further employed to compute observables such as emissivity and the degree of polarization due to synchrotron processes. Numerical benchmarks involving a relativistically expanding shell have been used to demonstrate the accuracy of our implementation against theoretical expectation. We adopt appropriate relativistic kinematic effects to estimate the observed degree of polarization and study its dependence on the viewing angles, $\theta_{\rm obs}$. We observe that the value of polarization degree saturates for larger viewing angles. For

gamma-ray energies, we obtain $\Pi \approx 56\%$ for a power-law distribution with $m = 3$, smaller than the theoretical upper limit of 75%. This effect of depolarization is consistent with values estimated by Lyutikov et al. (2003).

We have further applied our new framework to problems of astrophysical relevance involving either classical MHD or relativistic magnetized shocks. Two examples have been proposed.

1. *SN 1006.* In the first application, we have studied DSA and non-thermal emission in the context of SNRs with particular attention to SN1006. Our study of particle acceleration at classical MHD shocks using axisymmetric SNR simulations has shown that the average spectral index for particles is around $m = 2.1$, consistent with values obtained for strong shocks. The maximum spectral energy of 20 TeV obtained for the magnetic field of $\sim 8\mu$G is about a factor two times less than the upper limits obtained from fitting of observed spectra from SN 1006.

2. *Slab jet.* In the second application, we have investigated particle acceleration at shocks in a 2D relativistic slab jet. Unlike previous authors who employed a constant value for the spectral index of shocked particles, our method self-consistently determines the shock compression ratio and distinguishes between quasi-parallel or quasi-perpendicular shocks. This has shown to produce a considerable spreading in the electron spectral index (see Figure 12). Also, we observe knotty emission features for

X-ray energies and misaligned emissivity features, indicating the effects of oblique shocks. The polarization degree is also found to be larger at the jet/ambient interface, in agreement with radio and optical polarization signatures from 3C 264 (Perlman et al. 2010).

Forthcoming extensions of this work will aim at relaxing some of the simplifying assumptions adopted here. In particular, efforts will be taken to (i) incorporate energy dependence in the free parameter η for quasi-perpendicular relativistic shocks along with magnetic field amplification through feedback, (ii) include macro-particle back-reaction on the underlying fluid which can also account for modifications in the shock structure (Blasi 2002), and (iii) extend our framework to include spectral evolution of protons with an aim to compare leptonic and hadronic emission from jets. The ultimate goal of this framework would be to model multi-wavelength emission from AGN jets using 3D simulations.

Appendix A
Complete Analytic Solution for RMHD Shocks

Here we describe the steps used to derive the analytic solution that completely describes the RMHD shock with arbitrary orientation of magnetic fields. For the tests of planar shocks described in this paper, the inputs are the pre-shock conditions (region where the particle is initialized) and the shock speed (treated as an input parameter). Our aim is to obtain the scalar and vector quantities in the post-shock region (where the particle moves on crossing the shock). Without loss of generality we will assume here that the shock moves along the positive x axis.

Let us denote input quantities, U_a, in the pre-shock region with subscript a and the unknown post-shock quantities, U_b, with subscript b. In the lab frame, these quantities are related via the following jump condition across a fast magnetosonic shock with speed $v_{\rm sh}$:

$$v_{\rm sh}[U] = [F(U)]. \tag{77}$$

Here, $[q] = q_b - q_a$ denotes the jump across the wave and $F(q)$ is the flux for any quantity q. The set of jump conditions can be reduced to the following five positive-definite scalar invariants (Lichnerowicz 1976; Mignone & McKinney 2007):

$$[J] = 0 \tag{78}$$

$$[h\eta] = 0 \tag{79}$$

$$[\mathcal{H}] = \left[\frac{\eta^2}{J^2} - \frac{b^2}{\rho^2}\right] = 0 \tag{80}$$

$$J^2 + \frac{[p + b^2/2]}{[h/\rho]} = 0 \tag{81}$$

$$[h^2] + J^2\left[\frac{h^2}{\rho^2}\right] + 2\mathcal{H}[p] + 2\left[b^2\frac{h}{\rho}\right] = 0, \tag{82}$$

where $J = \rho\gamma_s\gamma(v_{\rm sh} - \beta^x)$ is the mass flux, γ_s is the Lorentz factor of the shock, and

$$\eta = -\frac{J}{\rho}(\mathbf{v} \cdot \mathbf{B}) + \frac{\gamma_s}{\gamma}B^x. \tag{83}$$

The specific gas enthalpy h is related to the gas pressure p and density ρ via an equation of state. The magnetic energy density, b^2 is related to the magnetic field $\mathbf{B}$ in the lab frame as

$$|b|^2 = \frac{|\mathbf{B}|^2}{\gamma^2} + (\mathbf{v} \cdot \mathbf{B})^2. \tag{84}$$

Following Mignone & McKinney (2007), we numerically solve the set of 3 × 3 nonlinear Equations (80)–(82) using the expression for the post-shock $\eta_b = \eta_a h_a/h_b$ from Equation (79). The solution of this closed set of equations gives us the three unknown scalars, namely the gas pressure p_b, density ρ_b, and magnetic energy density b_b^2 in the post-shock region.

The next step in describing the shock completely is to estimate the post-shock vector quantities, i.e., velocities $\boldsymbol{\beta}_b$ and magnetic fields $\mathbf{B}_b$. To estimate these, we use the exact Riemann solution for full set of RMHD equations (Giacomazzo & Rezzolla 2006). In particular, we obtain the tangential components of the velocity (β_b^y, β_b^z) in the post-shock region using the expressions presented in Appendix A of their paper. These expressions relate the tangential velocity components to the pre-shock quantities and only the post-shock pressure, p_b. Further, using the estimated tangential velocity components, we obtain the normal velocity β_b^x in the post-shock region using Equation (4.25) in Giacomazzo & Rezzolla (2006). With the knowledge of the post-shock velocity field, the magnetic fields in the post-shock region can be easily derived from the following jump conditions Giacomazzo & Rezzolla (2006):

$$\frac{J}{\gamma_s}\left[\frac{B^y}{D}\right] + B^x[\beta^y] = 0 \tag{85}$$

$$\frac{J}{\gamma_s}\left[\frac{B^z}{D}\right] + B^x[\beta^z] = 0, \tag{86}$$

where, $D = \rho\gamma$ is the proper gas density. Note that the magnetic field component normal to the shock front does not jump across the shock, i.e., $B_a^x = B_b^x$. The PYTHON code written to derive the analytic solutions for RMHD shock conditions will be made available upon request from the author.

Appendix B
Frame Transformation to NIF

In order to compute the spectral index of particle energy distribution as it passes the shock, one has to estimate the compression ratio in the shock rest frame. The compression ratio, r, is defined as the ratio of upstream to downstream velocities normal to the shock, and since the mass flux is conserved across the shock, it is also equivalent to the ratio of

densities across the shock for non-relativistic MHD:

$$r = \frac{\rho_2}{\rho_1} = \frac{\boldsymbol{v}_1 \cdot \hat{\boldsymbol{n}}_s}{\boldsymbol{v}_2 \cdot \hat{\boldsymbol{n}}_s}, \tag{87}$$

where the velocities $\boldsymbol{v}_{1,2}$ are obtained in the shock rest frame, which is defined in a unique way for the non-relativistic MHD case.

However, while treating RMHD shocks, one can have multiple shock rest frames (Ballard & Heavens 1991; Summerlin & Baring 2012). The NIF is the shock rest frame where the upstream velocity is normal to the shock front. The other shock rest frame often used in the case of RMHD flows is the de Hoffmann–Teller Frame (HTF) wherein the upstream velocity and magnetic fields are aligned with the shock at rest. Since the HTF is usually defined for sub-luminal shocks and does not exist for super-luminal shocks, we choose to work with the NIF as our preferred shock rest frame.

Given the shock speed, v_{sh}, normal to the shock direction, $\hat{\boldsymbol{n}}_s$ and both upstream and downstream states across the shock in the lab frame, we can transform to the NIF in a two-step process. The first step involves a Lorentz boost equal to the shock velocity and along its direction. Mathematically, any general four-vector $\boldsymbol{u}$ in the lab frame is related to $\boldsymbol{u}'$ in the Lorentz-boosted frame as follows:

$$\boldsymbol{u}' = \mathcal{L}(\beta_{\mathrm{bst}}, \hat{\boldsymbol{n}}_{\mathrm{bst}})\boldsymbol{u}, \tag{88}$$

where $\mathcal{L}$ is the symmetric Lorentz boost operator.

For the first step, $\beta_{\mathrm{bst}} = v_{\mathrm{sh}}$ and $\hat{\boldsymbol{n}}_{\mathrm{bst}} = \hat{n}_s$. The second transformation requires another Lorentz boost to transform the intermediate primed frame of reference to obtain the NIF. In this case, the boost has to be in the transverse direction to the shock and with a boost velocity $\beta_{\mathrm{bst}} = v_t'$, where, v_t' is the tangential velocity in the primed frame of reference. For 2D tests with planar shocks propagating along the x axis, the tangential velocity is the velocity along the y axis obtained in the intermediate prime frame.

With these two Lorentz boosts, we obtain the quantities across the shock in the NIF and then we can estimate the compression ratio as

$$r = \frac{\boldsymbol{\beta}_1^{\mathrm{NIF}} \cdot \hat{\boldsymbol{n}}^{\mathrm{NIF}}}{\boldsymbol{\beta}_2^{\mathrm{NIF}} \cdot \hat{\boldsymbol{n}}^{\mathrm{NIF}}} \tag{89}$$

$$= \frac{\rho_2 \gamma_2^{\mathrm{NIF}}}{\rho_1 \gamma_1^{\mathrm{NIF}}}. \tag{90}$$

ORCID iDs

Bhargav Vaidya (ID) https://orcid.org/0000-0001-5424-0059
Gianluigi Bodo (ID) https://orcid.org/0000-0002-9265-4081
Paola Rossi (ID) https://orcid.org/0000-0002-0840-4726

References

Achterberg, A., Gallant, Y. A., Kirk, J. G., & Guthmann, A. W. 2001, MNRAS, 328, 393
Aloy, M.-A., Gómez, J.-L., Ibáñez, J.-M., Martí, J.-M., & Müller, E. 2000, ApJL, 528, L85
Bai, X.-N., Caprioli, D., Sironi, L., & Spitkovsky, A. 2015, ApJ, 809, 55
Ballard, K. R., & Heavens, A. F. 1991, MNRAS, 251, 438
Birdsall, C., & Langdon, A. 2004, Plasma Physics via Computer Simulation (London: Taylor and Francis)
Blandford, R. D., & Königl, A. 1979, ApJ, 232, 34
Blandford, R. D., & Ostriker, J. P. 1978, ApJL, 221, L29
Blasi, P. 2002, APh, 16, 429
Bodo, G., Massaglia, S., Rossi, P., et al. 1995, A&A, 303, 281
Böttcher, M., & Dermer, C. D. 2010, ApJ, 711, 445
Daldorff, L. K. S., Tóth, G., Gombosi, T. I., et al. 2014, JCoPh, 268, 236
de la Cita, V. M., Bosch-Ramon, V., Paredes-Fortuny, X., Khangulyan, D., & Perucho, M. 2016, A&A, 591, A15
Del Zanna, L., Volpi, D., Amato, E., & Bucciantini, N. 2006, A&A, 453, 621
Drury, L. O. 1983, RPPh, 46, 973
Dulwich, F., Worrall, D. M., Birkinshaw, M., Padgett, C. A., & Perlman, E. S. 2009, MNRAS, 398, 1207
English, W., Hardcastle, M. J., & Krause, M. G. H. 2016, MNRAS, 461, 2025
Fromm, C. M., Perucho, M., Mimica, P., & Ros, E. 2016, A&A, 588, A101
Giacomazzo, B., & Rezzolla, L. 2006, JFM, 562, 223
Ginzburg, V. L., & Syrovatskii, S. I. 1965, ARA&A, 3, 297
Gómez, J. L., Martí, J. M., Marscher, A. P., Ibáñez, J. M., & Alberdi, A. 1997, ApJL, 482, L33
Gomez, J. L., Marti, J. M. A., Marscher, A. P., Ibanez, J. M. A., & Marcaide, J. M. 1995, ApJL, 449, L19
Hardcastle, M. J., & Krause, M. G. H. 2014, MNRAS, 443, 1482
Jokipii, J. R. 1987, ApJ, 313, 842
Jokipii, J. R., & Parker, E. N. 1970, ApJ, 160, 735
Jones, T. W., Ryu, D., & Engel, A. 1999, ApJ, 512, 105
Kardashev, N. S. 1962, SvA, 6, 317
Keshet, U., & Waxman, E. 2005, PhRvL, 94, 111102
Kirk, J. G., Guthmann, A. W., Gallant, Y. A., & Achterberg, A. 2000, ApJ, 542, 235
Kirk, J. G., & Reville, B. 2010, ApJL, 710, L16
Konigl, A. 1981, ApJ, 243, 700
Lichnerowicz, A. 1976, JMP, 17, 2135
Longair, M. S. 1994, High Energy Astrophysics, Vol. 2 (Cambridge: Cambridge Univ. Press)
Lyutikov, M., Pariev, V. I., & Blandford, R. D. 2003, ApJ, 597, 998
Marcowith, A., Bret, A., Bykov, A., et al. 2016, RPPh, 79, 046901
Marscher, A. P. 1980, ApJ, 235, 386
Mathews, W. G. 1971, ApJ, 165, 147
Micono, M., Zurlo, N., Massaglia, S., Ferrari, A., & Melrose, D. B. 1999, A&A, 349, 323
Mignone, A., Bodo, G., Massaglia, S., et al. 2007, ApJS, 170, 228
Mignone, A., Bodo, G., Vaidya, B., & Mattia, G. 2018, ApJ, 859, 13
Mignone, A., & McKinney, J. C. 2007, MNRAS, 378, 1118
Mignone, A., Zanni, C., Tzeferacos, P., et al. 2012, ApJS, 198, 7
Mimica, P., & Aloy, M. A. 2012, MNRAS, 421, 2635
Mimica, P., Aloy, M.-A., Agudo, I., et al. 2009, ApJ, 696, 1142
Miniati, F. 2001, CoPhC, 141, 17
Park, J., Caprioli, D., & Spitkovsky, A. 2015, PhRvL, 114, 085003
Parker, E. N. 1965, P&SS, 13, 9
Perlman, E. S., Biretta, J. A., Zhou, F., Sparks, W. B., & Macchetto, F. D. 1999, AJ, 117, 2185
Perlman, E. S., Padgett, C. A., Georganopoulos, M., et al. 2006, ApJ, 651, 735
Perlman, E. S., Padgett, C. A., Georganopoulos, M., et al. 2010, ApJ, 708, 171
Porth, O., Fendt, C., Meliani, Z., & Vaidya, B. 2011, ApJ, 737, 42
Reynolds, S. P., & Keohane, J. W. 1999, ApJ, 525, 368
Schneiter, E. M., Velázquez, P. F., Reynoso, E. M., & de Colle, F. 2010, MNRAS, 408, 430
Schwartz, S. J. 1998, ISSIR, 1, 249
Sironi, L., Keshet, U., & Lemoine, M. 2015, SSRv, 191, 519
Sironi, L., & Spitkovsky, A. 2009, ApJ, 698, 1523
Sironi, L., Spitkovsky, A., & Arons, J. 2013, ApJ, 771, 54
Skilling, J. 1975, MNRAS, 172, 557
Summerlin, E. J., & Baring, M. G. 2012, ApJ, 745, 63
Takamoto, M., & Kirk, J. G. 2015, ApJ, 809, 29
Taub, A. H. 1948, PhRv, 74, 328
Tregillis, I. L., Jones, T. W., & Ryu, D. 2001, ApJ, 557, 475
Vaidya, B., Mignone, A., Bodo, G., & Massaglia, S. 2016, JPhCS, 719, 012023
van Marle, A. J., Casse, F., & Marcowith, A. 2018, MNRAS, 473, 3394
Webb, G. M. 1989, ApJ, 340, 1112
Webb, G. M., & Gleeson, L. J. 1979, Ap&SS, 60, 335
Worrall, D. M., & Birkinshaw, M. 2005, MNRAS, 360, 926